Science Requirements Document

Version 1.3
April 1, 2010

for

FLAME DESIGN

a member of the ACME Flight Experiments

Principal Investigator
Richard L. Axelbaum, Washington University

Co-Investigators
David L. Urban, NASA GRC
Peter B. Sunderland, University of Maryland
Beei-Huan Chao, University of Hawaii

Project Scientist
Dennis P. Stocker, NASA GRC

EXECUTIVE SUMMARY

The majority of practical combustion processes involve nonpremixed combustion of hydrocarbons. These processes must be efficient and the resulting emissions low. For example, soot production, which can adversely affect efficiency, emissions, and equipment lifetime, must be controlled, and flame extinction must be avoided. Many methods have been considered to reduce soot, such as increasing strain rates and inert concentrations and reducing pressures, but these techniques generally weaken flames, leading to performance penalties and possible extinction. The proposed study considers a novel method of approaching combustion to address these concerns. The approach is termed *flame design*, as it takes a fundamental understanding of diffusion flames and, within the inherent constraints imposed, *designs* flames that best optimize efficiency and minimize pollutants.

Flame design involves affecting the basic structure of the flame in that the relationship between the temperature and concentration fields is varied to accomplish a stated objective. The method involves exchanging nitrogen (or any inert, including carbon dioxide) from the oxidizer stream to the fuel stream such that the stoichiometric mixture fraction, Z_{st}, can be varied with or without affecting adiabatic flame temperature, T_{ad}. The structure of a high Z_{st} flame is substantially different from that of the standard hydrocarbon/air flame, where Z_{st} is relatively low. By varying Z_{st} at constant T_{ad}, flames have been produced that are soot-free at any strain rate (permanently blue) and have extinction scalar dissipation rates up to 40 times those of their fuel-air counterparts.

The nitrogen exchange approach (or some variant of it) has been the subject of many studies by the PI and Co-Is (Du and Axelbaum, 1995, 1996, Chao *et al.*, 1998, Sunderland *et al.*, 2003, 2004, Liu *et al.*, 2005, Chen and Axelbaum, 2005, Kumfer *et al*., 2006, 2008, Santa *et al.*, 2007a, 2007b, Skeen *et al.*, 2009) and other investigators (Sung *et al.*, 1995; Lin and Faeth, 1996; Kang *et al.*, 1997; Hwang and Chung, 2001). Although these studies have been informative, they typically involved normal-gravity flames, where buoyancy and inherent strain complicated the interpretation of results. For example, these ambiguities have led to different theories to explain the phenomenon of permanently-blue diffusion flames. It is not known whether this phenomenon is due more to a change in the direction of convection across the flame or to a change in the detailed structure of the flame. This issue can be addressed by performing microgravity experiments because the unique character of nonbuoyant microgravity flames allows the effects of convection direction and flame structure to be independently varied. By ejecting fuel into an oxidizer in a buoyancy free system, the convective flow across the flame is unambiguously from fuel to oxidizer. Alternatively, by ejecting oxidizer into fuel, the flow is from oxidizer to fuel. Furthermore, the long residence times that can be obtained in the spherical flame geometry will allow for validation of a theory that predicts the sooting limits at the limit of infinite Damköhler number, *Da*.

Studies of the effect of Z_{st} on scalar dissipation rate at extinction have indicated that there is a unique Z_{st} where the flame is most resistant to extinction. These findings also suggest that by employing inert exchange to vary Z_{st}, the peak temperature can be shifted to coincide with the location of radical production, thus allowing the flame to burn at much lower temperatures. The optimum minimum temperature at extinction has led us to propose the concept of a pseudo-flammability limit for nonpremixed flames. Again, this fundamental information is most unambiguously demonstrated in quasi-steady, microgravity flames wherein the effects of flame structure can be systematically studied.

The proposed work will also allow, for the first time, a strain-free experimental study of the effects of Z_{st} on soot inception and flame extinction processes. Microgravity experiments will involve gaseous hydrocarbon diffusion flames supported on porous spherical burners and coflow burners.[1] Soot inception limits and flame extinction limits will be obtained as functions of Z_{st}, amount of inert, flow direction, and pressure. Extensive analytical and computational modeling will support the experimental investigation. Models will include gas-phase and burner-surface radiation.

Specifically, soot-inception limits in spherical flames will be measured by establishing a flame at a given Z_{st} and allowing peak temperature to decrease with time until the yellow luminosity is eliminated. The effect of flow direction across the flame will be studied by performing coflow experiments (desired) where the fuel issues into the oxidizer and oxidizer issues into fuel. Gas temperatures will be measured by thin film pyrometry and thermocouples to identify the soot-inception temperature.

In addition, soot volume fraction measurements will be made to evaluate the effects of Z_{st} and flow direction on soot formation and growth, and to better understand the phenomena of permanently-blue flames. Flame extinction limits will also be studied in a manner similar to that of soot inception limits, and temperatures near extinction will be measured.

The experiments and modeling will yield unique data that will allow for an understanding of how Z_{st} affects soot-inception and flame extinction and how Z_{st} can be used to design optimum flames. In addition, the effects of flow direction will also be studied and the importance of flow direction and flame structure to permanently-blue flames will be assessed. Finally, the proposed concept of a pseudo-flammability limit for nonpremixed flames will be evaluated and these limits will be ascertained for the test fuels. These results will be useful for the development of future combustion devices that will take advantage of oxygen enrichment technology to *design* more stable and less polluting flames.

[1] The coflow flame experiments are *desired*. This means that many critical goals of the experiments can be obtained without these experiments but they would add great value to the results.

TABLE OF CONTENTS

NOMENCLATURE

A	pre-exponential factor
a	acceleration
c_p	specific heat at constant pressure
C/O	local carbon/oxygen atom ratio
D	binary diffusion coefficient
Da	Damköhler number
d	diameter
E_a	activation energy
f_s	soot volume fraction
g	gravitational acceleration
h	specific enthalpy
K_{ext}	extinction strain rate
L	length
M	molecular weight
m	burner gas mass flow rate
R	universal gas constant
Ra	radiative loss rate
Ri	Richardson number
r	radial coordinate
T	temperature
t	time
T_{ad}	adiabatic flame temperature
T_{ext}	flame temperature at flame-extinction limit
u	flow velocity
V	diffusion velocity
W	molecular weight
X	mole fraction
Y	mass fraction
Z	mixture fraction
Z_{st}	stoichiometric mixture fraction

Greek and other symbols

ε	effective emissivity of the burner
κ	Planck mean absorption coefficient
λ	thermal conductivity
υ	stoichiometric coefficient
ρ	density
σ	Stefan-Boltzmann constant
τ_d	characteristic diffusion time
φ	porosity of the porous burner
$\dot{\omega}$	reaction rate

Subscripts

0	center of burner

b	burner
F	fuel
f	flame
g	gas species
k,j	k^{th}, j^{th} species
O	oxidizer
s	bulk material used to construct the burner
∞	supply gas

1 INTRODUCTION

1.1 Overview

Most flames found in industrial and residential applications are nonpremixed, i.e., the fuel and oxidizer are not mixed prior to entering the combustion chamber. There has been considerable effort to understand the fundamentals of this type of flame and much progress has been made. This understanding has, in general, led to improvements in combustion efficiencies and pollution reduction. The progress that has been made has been somewhat limited because the parameters that are readily varied in nonpremixed flames are limited. Mixing rates (scalar dissipation rates) and concentrations (typically in the form of fuel dilution) can be varied. The effects of mixing rate and dilution on reactant leakage (incomplete combustion), and soot formation have been well documented and improvements in nonpremixed combustion following these traditional approaches will continue to be made. Nonetheless, demands for increased combustion efficiency and significant reductions in pollution emissions will continue (Goldin, 1997). This study attempts to address the challenges and proposes a set of novel experiments that will demonstrate an approach to combustion that we term flame design. As will be shown, the understanding and potential benefits of this approach can only be unambiguously demonstrated by microgravity experiments.

What is flame design? It is an approach to flames that is conceptually similar to engineering design in that we start without preconceived notions of what constitutes a typical flame. We begin by considering what our objectives are for our nonpremixed flame and then design around the constraints imposed by a particular application. In general, complete combustion and minimal pollution from, for example, soot, unburned hydrocarbons (UHCs), CO, and NO_x are required. Flame temperature is a primary factor affecting combustion efficiency and pollutant formation. While higher temperature can ensure complete combustion, it also increases the amount of soot and NO_x in nonpremixed systems. Recognizing that the nonpremixed flame has a well-defined structure, and that the regions in the flame that affect radical production and pollutant formation are not necessarily the same, we ask the following question: *Can we design a flame that makes the most efficient use of the maximum temperature to ensure complete reaction, while at the same time minimizing pollutants such as soot, CO, UHCs and NO_x?* Herein we will limit our concerns to soot inception and flame strength (complete reaction), although this should be considered a paradigm study and other pollutants could be considered subsequently.

The question can be better appreciated by recognizing that the flame location is uniquely defined by stoichiometry in nonpremixed flames. For fuel burning in air the location of maximum temperature is not necessarily where it should be for a desired outcome, but is rather where stoichiometry forces it to be. This aside, we can now ask where we might want the peak temperature to be if it were possible to vary its location. To ensure complete reaction the peak temperature should be coincident with the location where radicals (e.g., OH, O and H) are

produced. This will ensure the most rapid radical production and the strongest flame for a given flame temperature. On the other hand, if production of soot is of concern, as is the case for gas turbines where the formation of soot can have a deleterious effect on turbine lifetimes, the maximum temperature should be far from the region of fuel pyrolysis, but near the region of soot/precursor oxidation. In this way we minimize the formation and maximize consumption of soot precursors. Are the requirements for a strong and soot-free flame compatible and, if so, can such a flame be designed? Recent studies have shown that the answer to both questions is yes.

An important aspect of flame design is that there is no preconception of the composition of the oxidizer mixture. In other words, we do not require the use of air. A justification for this is not required for NASA because the use of oxygen is standard practice in space applications. Nonetheless, a pervasive perspective of the combustion community is that any oxidizer other than air is not practical except in extreme situations. Is it realistic to suggest oxygen-enriched combustion when air is "free?" The suggestion that air is free for combustion is as erroneous as was the statement in the 1970's that solar energy is free. The true cost for modern combustion includes high capital and maintenance costs for pollution abatement equipment, which can run from 10-50% of the fuel costs. These costs are expected to increase steadily as the Environmental Protection Agency (EPA) and local governments impose more stringent requirements for air quality. Also, systems are often operated at less than optimum efficiency to minimize pollution or ensure flame stability. Thus, the question as to whether oxygen-enriched air is economical requires considering cradle-to-grave economics, which include all benefits that can be realized, e.g., the cost savings in capital equipment and maintenance, as well as the added cost of oxygen enrichment. The cost of oxygen enrichment has limited its applications, but studies as early as 1989 sponsored by the Gas Research Institute (Williams *et al.*, 1989) and the Department of Energy (Chace *et al.*, 1989) anticipated that oxygen-enriched combustion would be a critical combustion technology in the future. Recent progress in separation technologies has reduced the costs of oxygen and increased the viability of oxygen enrichment. Thus, long-range planning for combustion must include the possibility that oxygen-enriched air will be the oxidizer of the future.

Concerns about global warming have also brought the possibility of oxygen-enriched combustion to the forefront. Carbon dioxide is a greenhouse gas and is considered to be a primary source of global warming. The exhaust gas of air-fired combustors contains only 10-20% CO_2, the balance being primarily nitrogen. This dilute CO_2 stream is not conducive for capture, storage or reuse, and cost-effective methods of concentrating the exhaust are needed to make carbon capture and sequestration (CCS) a reality. One of the most promising methods of concentrating CO_2 in the flue gas is by combustion (e.g., of coal) with oxygen instead of air – oxy-fuel combustion. The oxygen can be diluted with recycled flue gas to control temperature, yielding a flue gas composed of over 95% CO_2 (Varagani et. al., 2004; Okazaki and Ando, 1997; Doctor *et al.*, 1997). With these high concentrations of CO_2, its direct recovery or sequestration becomes feasible. Nonetheless, there is a cost involved in oxygen separation and while oxy-fuel combustion is considered one of the most cost-effective ways of addressing greenhouse emissions, if other benefits are found for employing oxy-fuel combustion, implementation of greenhouse gas control will have a lower overall cost. This work will allow us to better understand oxy-fuel combustion and thus recommend alternative approaches to combustion that can reduce emissions, increase efficiencies, and reduce equipment costs.

Many industrial applications that require very high temperatures, for example, blast furnaces, already employ oxygen-enriched air. Argonne National Laboratories has been studying oxygen-enriched combustion in practical systems since the late 1990s. Researchers there proposed burning emulsified fuels in oxygen-enriched air as a means of reducing particulates in, for example, diesel engines (Callaghan *et al.*, 1998; Assanis *et al.*, 1993; Sekar *et al.*, 1991). As will be shown, the methodology employed in those applied studies is very similar to our inert exchange method. Furthermore, an entire book has been published on industrial applications of oxygen-enhanced combustion (Baukal, 1998). Clearly, the time is right for a fundamental program to evaluate the potential of oxygen enrichment in nonpremixed flames, and as will be shown below, studies in long-duration microgravity are required to understand the effects and ultimate potential of oxygen enrichment. The link between these applied studies and the proposed study is that oxygen enrichment and fuel dilution have a strong effect on the stoichiometric mixture fraction, Z_{st}.

1.2 Background on Flame Design: The Effects of Z_{st}

Sooting Limits

Du and Axelbaum (1995) showed experimentally and numerically that Z_{st} can have a profound effect on soot inception. Z_{st} characterizes the flame structure and is given by

$$Z_{st} = (1+Y_{F,\infty} W_O \nu_O / Y_{O,\infty} W_F \nu_F)^{-1} , \qquad (1.1)$$

where Y is mass fraction, W is molecular weight, ν is the stoichiometric coefficient, and the subscript O refers to oxidizer and F to fuel. To understand the isolated effects of flame structure, Z_{st} was varied while maintaining a constant adiabatic flame temperature T_{ad}. This was accomplished by recognizing that diffusion flames are constrained to burn stoichiometrically (in the limit of infinite Damköhler number), which implies that for an equidiffusional system with a given stoichiometry, T_{ad} is uniquely defined.

For example, the stoichiometry of an ethylene diffusion flame yields

$$C_2H_4 + 3O_2 + \nu_{N2} N_2 \rightarrow \text{products} . \qquad (1.2)$$

For ethylene burning in air, the stoichiometric coefficient for the inert is $\nu_{N2} = 11.28$ and the adiabatic flame temperature is $T_{ad} = 2370$ K. Provided that the stoichiometry in this equation is maintained, the nitrogen can be introduced with the fuel, oxygen or a combination of both, with no impact on T_{ad}. In other words, T_{ad} of a fuel mixture containing 1 mole of C_2H_4 and 11.28 moles of N_2 burning in pure oxygen is the same as that of pure C_2H_4 burning in air.

The effects of flame structure on soot particle inception can be strongly dependent on Z_{st}. In Fig. 1.1 the flame-sheet solution is plotted for $Z_{st} = 0.064$ (a) and $Z_{st} = 0.78$ (b). Fig. 1.1 indicates that in the ethylene/air flame the mean ethylene concentration is large in the high temperature region, i.e., conditions are favorable for soot inception. However, in the diluted-ethylene/oxygen flame, the mean concentration of fuel in the high temperature region is low. Thus, fuel-pyrolysis chemistry is inhibited at high Z_{st}. This implies that the conditions in the ethylene/air flame are more conducive to soot inception than are those in the diluted ethylene-oxygen flame, even though they both have the same adiabatic flame temperature.

Experimental results confirm that as Z_{st} is increased, soot inception is suppressed. Significantly, at high Z_{st} the flames remain blue even when strain rates are small in counterflow flames or as heights approach infinity in coflow flames. G.M. Faeth coined the name permanently-blue to describe such flames (Lin and Faeth, 1996).

While there is clear evidence of the importance of Z_{st} on soot inception, there have been different interpretations of this behavior (Sugiyama, 1994; Du and Axelbaum, 1995, Lin and Faeth, 1996). Sugiyama and Faeth both maintained that the effect is primarily hydrodynamic. In the context of Z_{st} and counterflow flames, this argument can be understood as follows: referring to Fig. 1.2a we see that for $Z_{st} < 0.5$ the streamlines are directed from the oxidizer to the fuel. Thus, soot particles are produced on the fuel side of the flame and are convected into increasingly rich regions. For $Z_{st} > 0.5$, shown in Fig. 1.2b, the streamlines are directed from fuel to oxidizer so that soot particles can be rapidly oxidized.

Axelbaum *et al.* have argued that while flow direction will certainly impact soot growth, at the *sooting limit* the process is not one of heterogeneous soot growth, but rather soot inception, which occurs through gas-phase chemistry. For the gas-phase reactions of soot inception, flow direction is less important. A diffusion flame is a diffusive-convective system and this balance allows for changes in the convective direction without substantial changes in the flame response. Furthermore, since the soot inception zone is finite, it is indeed possible to produce soot when $Z_{st} > 0.5$

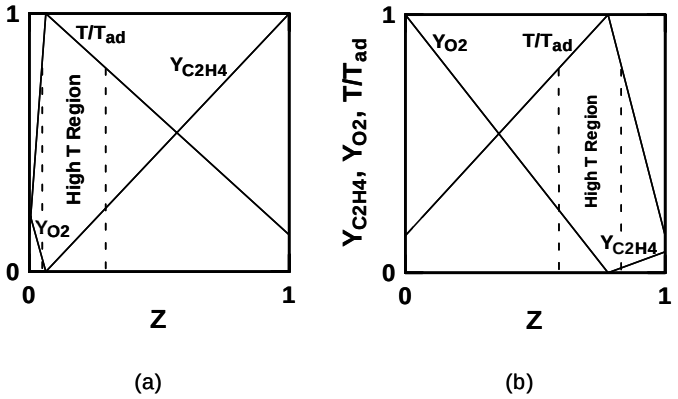

Figure 1.1. Schematic diagram of the flame sheet solution for fuel, oxidizer and temperature profiles in mixture fraction space for (a) an ethylene-air diffusion flame, Z_{st} = 0.064, and (b) a diluted-ethylene/oxygen flame, Z_{st} = 0.78. (Du and Axelbaum, 1995).

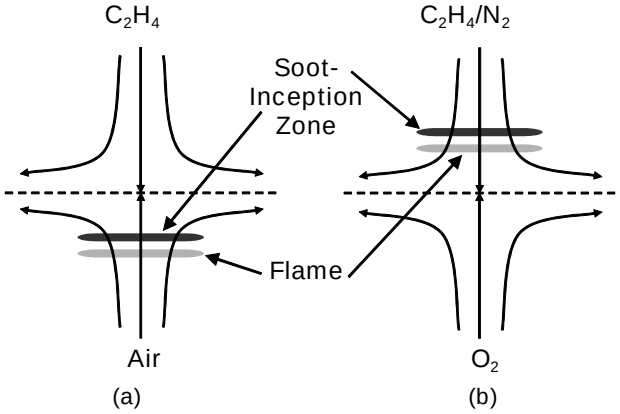

Figure 1.2. Schematic representation of counterflow flames with (a) $Z_{st} < 0.5$ such that the flame is on the oxidizer side of the stagnation plane and the flow is from the soot inception region to the fuel source and (b) $Z_{st} > 0.5$ such that the flame is on the fuel side of the stagnation plane and the flow is from the soot inception region to the oxidizer source. (Sunderland *et al.*, 2003).

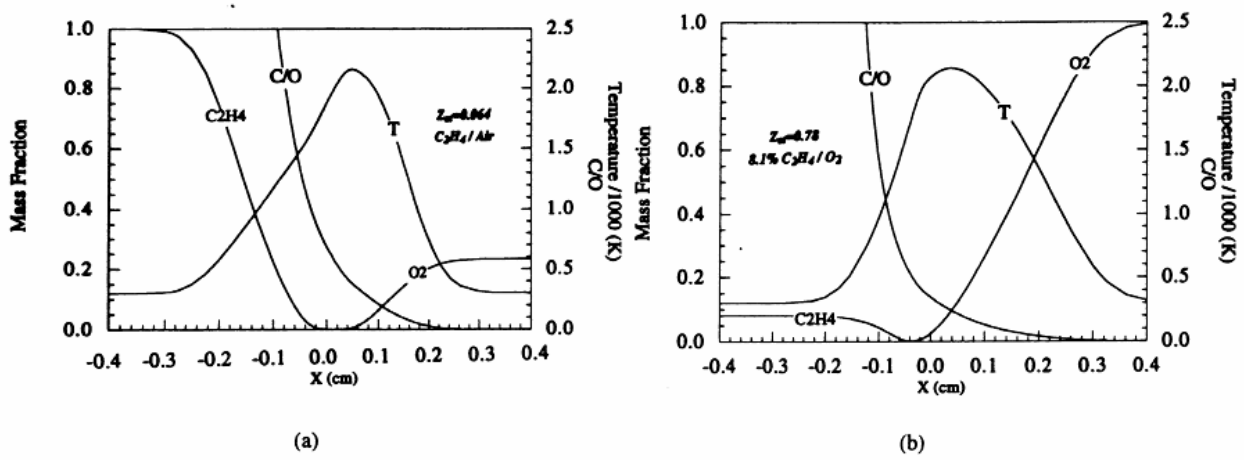

Figure 1.3. Numerical results for ethylene/air counterflow diffusion flames for (a) Z_{St} = 0.064 and (b) Z_{St} = 0.78, at strain rate of 100 s^{-1}. (Du and Axelbaum, 1995).

Z_{st} the oxygen has shifted deep into the fuel side of the peak temperature. This shift narrows the soot formation zone. Du and Axelbaum (1995) suggested it may be possible to obtain soot-free conditions for many fuels if the structure of the flame can be adjusted to the extent that significant oxidizer exists on the fuel side of the flame at a low enough temperature. Studies have reported that at temperatures below 1250 K soot does not form (Gomez *et al.*, 1987, Santoro *et al.*, 1987, Sunderland *et al.*, 1995) and, as seen from Fig. 1.3, at about 1250 K the local C/O ratio is less than unity, suggesting that soot cannot form in this flame for realistic residence times. Faeth and co-workers applied nitrogen exchange and their data support the above hypothesis in that they were able to obtain permanently-blue flames at low strain rates ($<100\ s^{-1}$) for acetylene, propylene and butadiene.

Resolution of this issue is of significance to our understanding of soot inception in diffusion flames, not only because permanently-blue flames are of fundamental importance, but also because if the basic structure of the flame has a strong effect on soot particle *inception*, to date this has not been sufficiently studied.

With normal gravity nonpremixed flames, e.g., coflow and counterflow flames, it is not possible to resolve this issue because the direction of the flow field and flame structure cannot be varied independently. Consequently, there is an inherent ambiguity in the mechanism responsible for soot suppression. A key advantage of microgravity is that buoyancy is not present to influence the convective flow field and thus the direction of convection in laminar diffusion flames can be unambiguously controlled. This is true for both spherical coflow diffusion flames. An additional advantage of the spherical diffusion flame is that it is nearly one-dimensional and can be easily formed in microgravity by ejecting one reactant from a porous sphere into a quiescent environment of the other reactant. Furthermore, the range of residence times for spherical flames can be significantly larger than for normal-gravity flames owing to the lack of buoyancy. No comparable experiments exist in normal gravity. The one-dimensional flame is also the most basic flame. While premixed flames can easily be made one-dimensional in normal gravity, nonpremixed flames cannot because the fuel and oxidizer are initially separate and buoyancy does not allow the gases to mix in one dimension. Thus, studies of soot inception and flame extinction in one-dimensional flames are of fundamental importance and the data generated from microgravity experiments will yield a valuable database wherein the interplay of kinetics, transport, radiation heat transfer and thermophoresis are revealed.

Flame Extinction

Although T_{ad} is the same for the two flames of Fig. 1.2, their response in terms of flame extinction is very different (Du and Axelbaum, 1996). Extinction strain rate limits at a given T_{ad} tend to increase with Z_{st}. For example, the measured extinction strain rate K_{ext} for methane-air flames (Z_{st} = 0.055) is 393 s^{-1} while for the diluted methane-oxygen flame (Z_{st} = 0.78) it is 883 s^{-1}. This increase results from the shift of the O_2 profile into regions of higher temperature. This increases the OH and O production rates in this region, yielding stronger flames. The shift can result in more than a 100 °C difference in the extinction temperature. This contrasts with the data of Ishizuka and Tsuji (1981), which suggested that there is a single limit temperature that constrains the extent of dilution that a flame can sustain. The results of Du and Axelbaum (1996) suggest that the lowest extinction limit temperature for stable burning corresponds to the condition where the OH and O production zones are centered on the location of peak temperature. Thus achieving the lowest temperature for stable burning of a diffusion flame requires the flame to be *redesigned*. An undesigned flame does not use the peak temperature

effectively because the peak temperature must be high enough to ensure that the temperature at the location of radical production is sufficiently high. The offset distance between the peak temperature and the peak radical production is directly related to the global structure of the flame (Z_{st}). This is because the critical branching reaction

$$H + O_2 \rightarrow OH + O \tag{1.3}$$

has a reaction rate $\dot{\omega}$ given by

$$\dot{\omega} = [H][O_2]\, A \exp(-E_a/RT)\,, \tag{1.4}$$

where A is the pre-exponential factor, R the universal gas constant, and E_a the activation energy.

As seen in Fig. 1.4a, the maximum reaction rate does not inherently reside at the location of peak temperature for a methane-air flame (Z_{st} = 0.55) but rather is displaced to the oxidizer side (Du and Axelbaum, 1996). Good *design* would dictate that the peak temperature should be at the location of peak radical production and this is confirmed by the results of Fig. 1.4b for a diluted methane-enriched air flame (Z_{st} = 0.65). These two flames are at their extinction strain rates. The temperature at extinction for Fig 1.4a is 1840 K while that of Fig. 1.4b is 1740 K.

This finding has important implications for control of NO_x as well because if stable ethylene flames can be sustained at temperatures 100 °C less than that in ordinary flames, the flames can be operated at lower temperatures and with less NO_x. Furthermore, while in these experiments the nitrogen was redirected into the fuel, in practice exhaust gas could be used instead, further reducing NO_x formation.

1.3 Ground-based Microgravity Research

In the following we summarize ground-based results in microgravity for several peer-reviewed journal papers by the investigator team. These works were conducted as preliminary studies related to the flight-based experiments. The summaries below include experimental details that are related to the flight-based experiments.

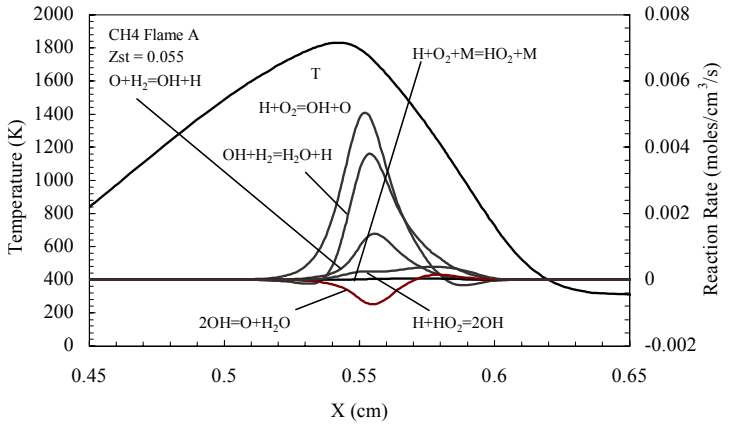

(a)

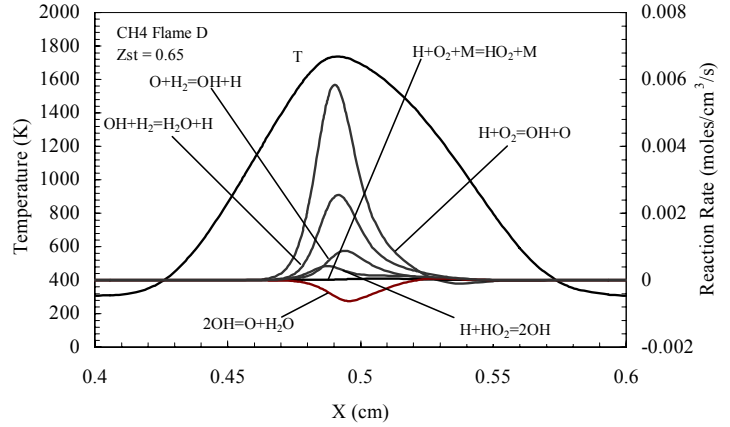

(b)

Figure 1.4. Reaction rate profiles for the primary radical production reactions and temperature in the physical coordinate for (a) Z_{st} = 0.55 (methane-air), and (b) Z_{st} = 0.65 (diluted methane-enriched air flame). (Du and Axelbaum, 1996).

Effects of Structure and Hydrodynamics on the Sooting Behavior of Spherical Microgravity Diffusion Flames (Sunderland *et al.*, 2003)

To study the effects of flame structure and flow direction on the sooting behavior of diffusion flames, microgravity spherical flame experiments were conducted in the NASA Glenn 2.2 s drop tower using a general-purpose combustion rig. The rig included a windowed pressure vessel and a burner that consisted of a 6.4 mm diameter porous sphere. The sphere was supported and fed by a 1.6 mm stainless steel tube attached with epoxy. All tests were conducted in quiescent ambient gas at 0.98 bar. To minimize disturbances, the flames were ignited immediately after release into microgravity using a spring-loaded Nichrome wire. Gas-phase temperatures were measured with an uncoated B-type thermocouple. The thermocouple was held in a fixed position

TABLE 1.1. Test conditions and measured peak temperatures for the four flames of Sunderland *et al.* (2003).

		Prescribed				Measured		
Flame	Ambient	X_{C2H4}[a]	X_{O2}[a]	Z_{st}	m_b, mg/s	d_f, mm	T_{raw}, K	$T_{corrected}$, K
(a)	Oxidizer	1	0.21	0.064	1.51	29.3	1302	1399
(b)	Oxidizer	0.08	1	0.78	18.6	18.8	1760	1923
(c)	Fuel	1	0.21	0.064	22.2	24.7	1907	2111
(d)	Fuel	0.08	1	0.78	5.18	31.3	1300	1385

[a]Balance is N_2.

for each test so that the slowly expanding flame passed the junction approximately 0.2 s before drop termination.

The four flames considered are summarized in Table 1.1. The ethylene consumption rate for all flames was held constant at 1.51 mg/s. All four flames have the same adiabatic flame temperature of 2370 K. The peak temperatures of the four flames measured near the end of the drop are tabulated in Table 1.1 in both raw and radiation-corrected forms. Despite the uniform T_{ad} = 2370 K and ethylene consumption rates, the flames have disparate peak temperatures, as discussed below.

The flames were imaged through the chamber window using a color CCD camera. Figure 1.5 shows color images, captured just prior to drop termination, of representative flames for the four conditions considered. The final diameters of the present flames are evident in Fig. 1.5. Recalling that the flames have the same ethylene consumption rate, flames (b) and (c) are smaller than the others since they involve diluted burner gas and pure ambient gas.

Figure 1.5 reveals that the sootiest flame is flame (c), with air injecting into ethylene. This is expected since both flame structure (small Z_{st}) and convection direction (towards fuel) promote soot formation and the peak temperature is the highest. Conversely, one would expect the least soot in flame (b) since it has a large Z_{st}, its convection is towards the oxidizer, and its temperature is lower. Indeed, flame (b) is soot free. The effect of convection direction on soot formation at constant Z_{st} is observed in flames (a) and (c). These flames both have Z_{st} = 0.064 (favoring soot formation) but opposite convection

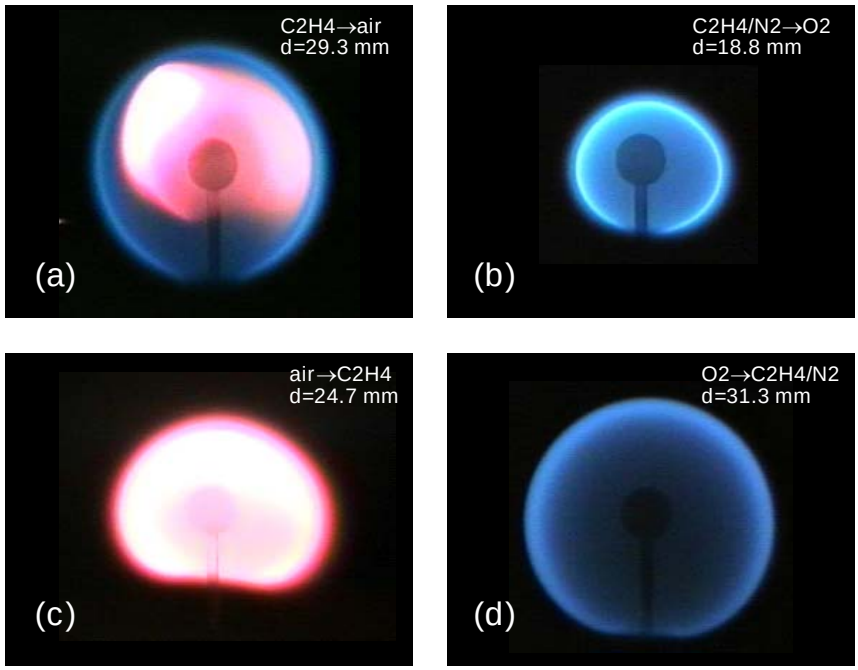

Figure 1.5. Color images of representative flames at the end of the 2 s drop for Flames (a) – (d) of Table 1.1. The scale is revealed by the 6.4 mm spherical burner. (Sunderland *et al.*, 2003).

directions. Particles formed in flame (a) are convected towards the oxidizer where they appear to completely oxidize. The presence of yellow luminosity in flame (a) suggests that convection into the oxidizer suppresses soot growth but does not eliminate soot inception. Flame (c) has a high flame temperature and the soot particles formed at the flame are convected towards the fuel, allowing for remarkable soot growth.

The effect of flame structure (Z_{st}) on soot formation is most apparent in flame (d), where convection is directed towards the fuel (favoring soot formation). Structure is seen to have a significant effect, yielding a blue flame at $Z_{st} = 0.78$. Blue flame conditions are realized in flame (d) despite its convection towards the fuel, which would suggest favorable conditions for soot growth. Flames (a) and (d) allow for a clear indication of the relative importance of structure and convection direction on the phenomena of permanently blue flames. The flames have almost identical peak temperatures, but convection favors soot oxidation in flame (a) and soot formation in flame (d). Flame (a) produces soot while flame (d) does not, indicating that flame structure is responsible for the soot free conditions of flame (d). These results attest to the dramatic effects of Z_{st} on soot inception.

The main conclusion of this paper was that flame structure, quantified by Z_{st}, had a profound effect on soot production. Soot-free conditions were observed at high Z_{st} and sooting conditions were observed at low Z_{st} regardless of convection direction. Convection direction was found to have a smaller impact on soot inception, and had a suppressive effect on soot formation when convection at the flame sheet was directed towards the oxidizer.

Sooting Limits of Microgravity Spherical Diffusion Flames in Oxygen-Enriched Air and Diluted Fuel (Sunderland *et al.*, 2004)

In this paper the sooting limits of spherical diffusion flames were studied in microgravity as a function of Z_{st}. The importance of flame structure and flow direction on the sooting limits were evaluated and this led to a proposal of the following criteria for soot inception to occur in nonpremixed flames: that there be a region in the flame where three quantities – C/O atom ratio, temperature, and scalar dissipation rate – are above certain critical values. The key points are summarized below.

Preliminary measurements of soot-inception limits in microgravity were performed in the drop facilities at NASA Glenn in an extension of our work above. The microgravity tests were conducted as described above. Sooting limit conditions were defined as conditions for which yellow luminosity was visible at the end of the drop, but for which a small reduction in X_{C2H4} or X_{O2} in the supply gases yielded flames devoid of yellow.

The characteristic time in this paper was the residence time required for a parcel of gas to convect from the burner surface to the flame sheet. In subsequent work from our group, scalar dissipation rates also are considered. Spherical flames with short residence times (ca. 10 ms or less) encounter hydrodynamic suppression of soot akin to that observed in counterflow flames. Flames with long residence times (ca. 0.5 s or more) are unlikely to reach steady conditions within 2.2 s and have large radiative losses. To evaluate these concerns we introduce here a characteristic residence time, t_{res}, defined as the mass of gas contained between the flame and the burner surface divided by the burner mass flow rate. In subsequent work residence time is taken as the convection time predicted by the numerical model.

The general behavior of these flames resembles that described in Sunderland *et al.* (2003), although here only flames near sooting limits are considered. The diameters and total radiative emissions increased throughout the 2.2 s drops for all flames, and when yellow emission was

observed its intensity decreased with time. Exchanging N_2 from the ambient gas to the burner effluent at constant T_{ad} decreased the flame size, sphericity (owing to flow non-uniformity generated by the porous burner), and the characteristic time to reach steady state, and increased the peak brightness.

Seventeen sooting limits were identified. Normal and inverse flames were represented, with a wide range of reactant mole fractions, Z_{st}, and T_{ad}. Ethylene consumption rate was 1.5 mg/s for all flames. Four representative flames at or near their sooting limits are shown in Fig. 1.6. These flames represent both convection toward oxidizer (normal flames) and convection toward fuel (inverse flames). The flames of Fig. 1.6b and 1.6d are considered here to be at the experimental sooting limits at 2.2 s because a small reduction in reactant concentration yields blue conditions. Note that soot, when present, appears inside the flame sheet for normal flames and outside for inverse flames.

The sooting limits are plotted in Fig. 1.7. These axes are motivated by a simplified model. Under the hypothesis that soot formation requires a region where local C/O ratio and T exceed their critical values (and where strain rate is sufficiently low), and employing the Burke-Schumann assumptions, Y_C, Y_O and T are linear in Z. This leads to the prediction of a linear relationship between Z_{st} and T_{ad} at the sooting limits.

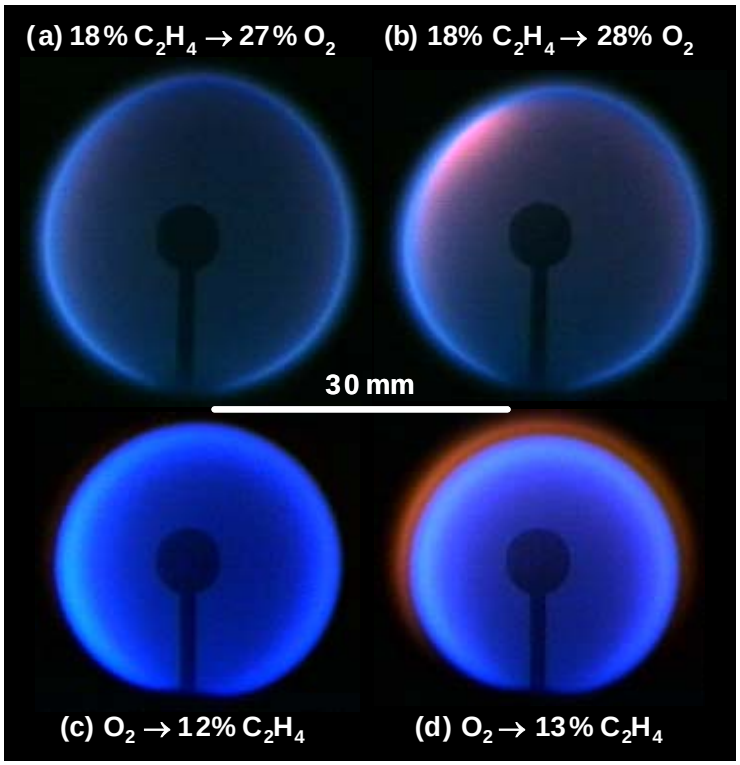

Figure 1.6. Color images of limit flames and corresponding near-limit flames for fuel-into-oxidizer: (a) and (b), and oxidizer-into-fuel: (c) and (d). Experiments performed in the NASA 2.2 s drop tower. (Sunderland *et al.*, 2004).

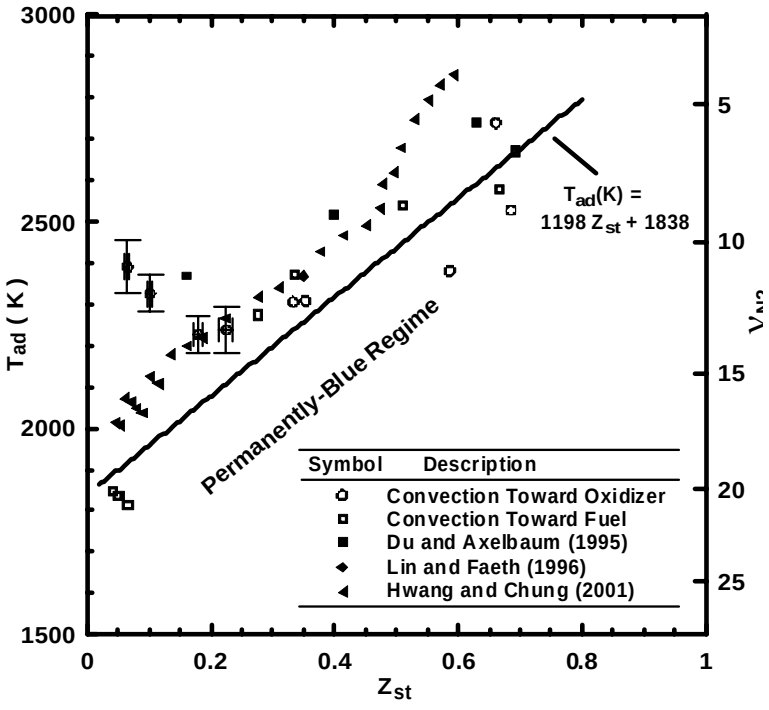

Figure 1.7. Sooting limit in terms of stoichiometric mixture fraction and adiabatic flame temperature. (Sunderland *et al.*, 2004).

The data in Fig. 1.7 define a region of permanently-blue conditions. Error bars are included for the four flames at the lowest Z_{st} and these flames are excluded from the fit shown. Among the present flames these have the longest residence times (all in excess of 0.5 s) and the most unsteady diameters. These conditions also are associated with large gas-phase radiative losses, leading to a large reduction of actual peak temperature below T_{ad}. This is confirmed by past measurements (Sunderland *et al.*, 2003), which found that a similar flame had a peak temperature that was reduced 970 K from its T_{ad}, whereas flames with shorter t_{res} had much smaller reductions.

Figure 1.7 shows that convection direction has no measurable effect on the sooting limits of these spherical flames. Although soot formation can be suppressed by decreasing residence time (or increasing strain rate), the present flames have residence times that are longer than those of past counterflow flames. Several normal-gravity sooting limits also are included in Fig. 1.7. Conditions identified as sooting limits in normal-gravity tests yield yellow flames in the spherical configuration. This is attributed to the intrusion of strain in the normal-gravity tests.

In summary, this study found that soot-free conditions were favored at increased Z_{st} and there was no observed effect of convection direction on the sooting limits. The sooting limits follow a linear relationship between adiabatic flame temperature and Z_{st}, with Z_{st} accounting for a variation of about 700 K in the sooting limit adiabatic flame temperature. While heat release rate was held constant, the flames had different sizes and residence times. These flames can be affected by transient size, imperfect sphericity, burner heating, radiation, and thermophoresis. Unfortunately, these flames are limited by the 2.2 s test times. For flames with characteristic residence times below 0.5 s, effects of transient flame development, including that due to reactant accumulation (King, 1996, Tse *et al.*, 2001), and gas-phase radiation (Atreya and Agrawal, 1998, Tse *et al.*, 2001) are expected to be small. But for longer residence time flames, the restriction of the existing ground-based facilities precludes unambiguous microgravity results.

Numerical and Experimental Observations of Spherical Diffusion Flames (Santa *et al.* 2007b)

This paper presented a numerical model of the spherical diffusion flames. In the model a gaseous reactant is injected from the porous spherical burner at temperature T_b into an infinite quiescent environment of the other reactant at temperature T_∞. The flow field is assumed to be spherically symmetric. The numerical code is a modification of the PREMIX code (Kee *et al.*, 1987), adapted to a diffusion flame in a spherical geometry and allowing for optically thick radiative heat losses. Conservation of mass, energy and gas species are solved, as follows:

$$\frac{\partial \rho}{\partial t} + \frac{1}{r^2}\frac{\partial (r^2 \rho u)}{\partial r} = 0 \ , \tag{1.5}$$

$$\rho c_p \frac{\partial T}{\partial t} = \frac{1}{r^2}\frac{\partial}{\partial r}\left(r^2 \lambda \frac{\partial T}{\partial r}\right) - \rho u c_p \frac{\partial T}{\partial r} - \sum_{k=1}^{K}\left(\rho c_{p,k} Y_k V_k \frac{\partial T}{\partial r} + h_k \omega_k Y_k\right) - Ra \ , \tag{1.6}$$

$$\rho \frac{\partial Y_k}{\partial t} = -\frac{1}{r^2}\frac{\partial}{\partial r}\left(r^2 \rho Y_k V_k\right) - \rho u \frac{\partial Y_k}{\partial r} + W_k \omega_k Y_k \ , k = 1, 2, \cdots, K \ , \tag{1.7}$$

subject to these boundary conditions:

$$r = r_b : T = T_b \ ; \ Y_k (u + V_k) = u Y_{k,0} \ , k = 1, 2, \cdots, K \ , \tag{1.8}$$

$$r \to \infty : T \to T_\infty \; ; \; Y_k \to Y_{k,\infty} \; , k = 1, 2, \cdots, K \, , \tag{1.9}$$

Because thermocouple measurements in the 5 s drop facility showed no significant increase in burner surface temperature during the drop, T_b was taken to be constant at 300 K. In addition, the results indicate that after 5 s the thermal field reached a radius of 9 cm from the center of the burner. Thus, while the computations assumed a finite domain (r_{wall} = 100 cm), it was effectively infinite and the results were not affected by this assumption.

Radiation was considered to be optically thick and caused only by the participation of CO_2, H_2O and CO. The radiative properties of these gases were formulated by a statistical narrow-band model with a spectral bandwidth of 25 cm^{-1}. The emissivities were extracted from the line-by-line values given by the HITRAN database (Rothman *et al.*, 2003). To account for the angular variation of the radiation intensity, the discrete ordinates method was employed, with a discrete representation that included 20 different directions. The rate of radiative heat transfer was then evaluated by integrating over all directions using Gaussian quadrature.

Conventional finite difference techniques with non-uniform mesh spacing were adopted for the discretization of the differential equations. The transient terms were expressed by a forward difference formula, the diffusive terms by a central difference formula, and, for better convergence, the convective terms by an upwind difference formula. The discretized equations were solved by Sandia's Twopnt package (Grcar, 1992), which uses Newton's method to solve transient and steady-state boundary value problems. The chemical reaction rates, the thermodynamic properties, and the transport properties were evaluated by Chemkin and Transport software (Kee *et al.*, 1988, 1989). The kinetics data were provided by GRI-Mech 3.0, which contains 53 species and 325 reactions (Smith *et al.*, 2007). The number of grids was varied until the solution did not change with further addition of grids. The time step was adjusted until the solution converged.

Following the approach adopted in Tse *et al.* (2001), the initial (ignition) conditions for the transient cases were prescribed as the steady-state solutions of flames without radiation and with the same outer boundary values, but with the outer boundary brought to 1.2 cm from the burner exit. This led to a thin high-temperature ignition source near the burner surface, which is consistent with the conditions that would exist when a diffusion flame is first established after ignition.

Computations were performed for ethylene flames (a) – (d) of Sunderland *et al.* (2003). While the trends for flames (a), (b), and (d) predicted by the model closely resemble those of the experiments, the model predicts larger flames. The exact source of the discrepancy remains unclear, but it could arise from thermal and mass diffusion properties that are too low in the model or from experimental flow rates that are lower than reported. Transport properties are based on the Lennard-Jones potential model (Hirschfelder *et al.*, 1964), which can underpredict transport properties of light species by up to 25% (Paul and Warnatz, 1998, Middha *et al.*, 2002).

To evaluate the effect of assumed transport properties, the thermal and mass diffusion properties in the model were varied. Because both transport properties were increased, the Lewis number and the adiabatic flame temperature were unchanged. The results for an increase of 30% for flames (a), (b), and (d) are shown in Fig. 1.8. The flame radius from the model was assumed to be the radius of the peak temperature. Flame (c) was not included in Fig. 1.8 owing to soot obscuration. The agreement between model and experiment in Fig. 1.8 is good.

All four flames initially grew with time, but flames (b) and (c) approached steady state more rapidly than flames (a) and (d) because of their high flow velocities and low residence times.

Predictions of transient peak flame temperatures for the four ethylene-fueled flames are shown in Fig. 1.9. Due to gaseous radiative heat loss the peak temperatures decrease with time except near ignition. Although these four flames have the same adiabatic flame temperature (2370 K), the temperatures of flames (a) and (d) are predicted to be markedly lower than those of flames (c) and (b). Flames (a) and (d) have roughly double the radii of the others, which leads to increased radiative losses.

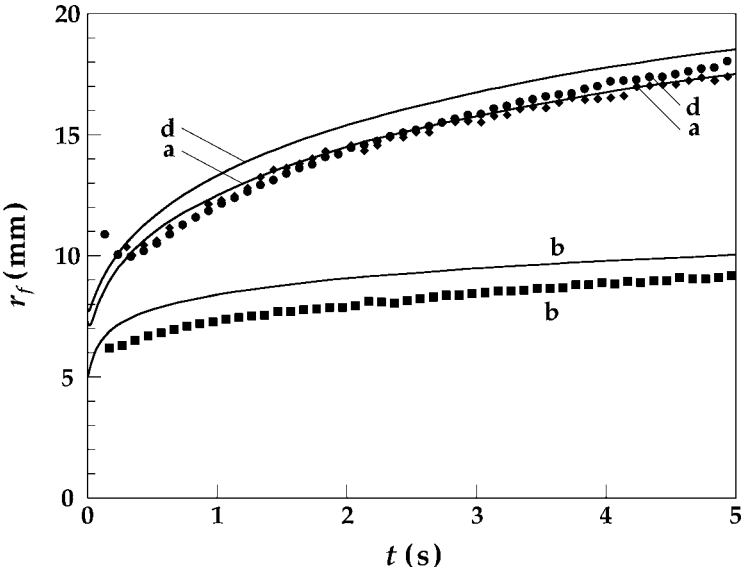

Figure 1.8. Predicted (curves) and measured (symbols) flame radii for ethylene flames (a), (b), and (d). Measurements were obtained in the 5 s drop facility. (Santa *et al.*, 2007b).

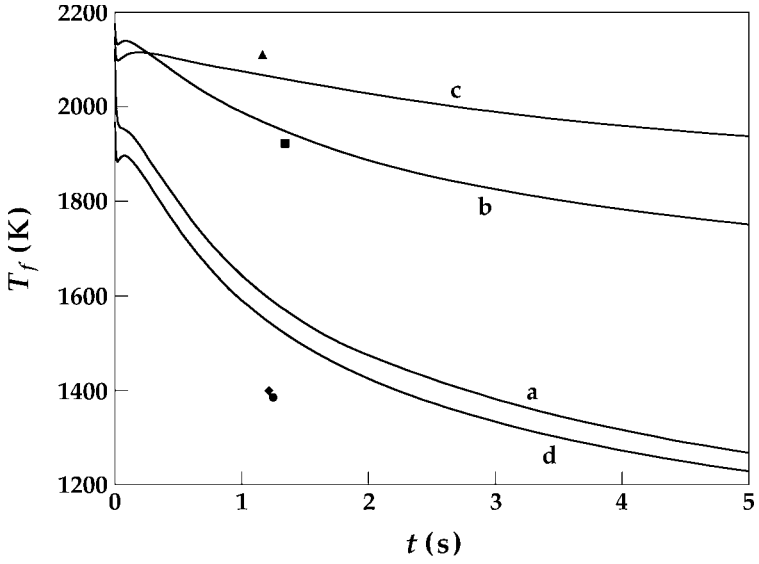

Figure 1.9. Evolution of peak temperature for ethylene flames (a) – (d). The curves are model predictions while the symbols are thermocouple measurements of Sunderland *et al.* (2003). (Santa *et al.*, 2007b).

Also shown in Fig. 1.9 are peak temperatures for these four flames as measured with thermocouples in the 2.2 s drop tower, followed by radiation corrections. The agreement between modeled and measured temperatures is within experimental uncertainties for flames (b) and (c). The numerical predictions in the other two flames significantly over-predict the measured temperatures and this probably arises from different ignition conditions in the model and the experiment. Such differences are not evident for flames (b) and (c), where effects of ignition are convected outward more rapidly.

In summary, this manuscript found that the low flow velocities and long residence times in these diffusion flames lead to enhanced diffusive effects. For example, the results show that the ambient gas Lewis number can have a strong effect on flame temperature – a 10% decrease in Lewis number can increase the steady-state flame temperature by 200 K. The strong effect of Lewis number is supported by temperature measurements. Furthermore, the large diffusion

distances associated with these flames can lead to unusual steady-state compositions near the outer boundary when hydrocarbon fuel is supplied from the ambient, as decomposition products can diffuse to the outer boundary and result in a loss of chemical enthalpy from the system.

Transient predictions of flame sizes were significantly larger than those observed in microgravity experiments. Agreement could not be obtained unless the model's thermal and mass diffusion properties were increased by 30%. Clearly further study, preferably under long duration microgravity, is needed to determine the exact cause of the discrepancy between experimental and numerical flame sizes.

Radiative Extinction of Gaseous Spherical Diffusion Flames in Microgravity (Santa *et al.*, 2007a)

Radiative extinction is unlikely in normal gravity because buoyancy increases with flame size, and under conditions where radiative extinction might otherwise occur, buoyancy enhances mixing and reduces residence times. On the other hand, radiative extinction can be important in microgravity and its improved understanding should contribute to spacecraft fire safety. Microgravity experiments allowed the first observation of radiative extinction, this being for droplet combustion (Dietrich *et al.*, 1996, Nayagam *et al.*, 1998). Santa *et al.* (2007a) presents observations of radiative extinction in gaseous spherical flames.

As described above, the experiments were conducted in microgravity in the NASA Glenn 2.2 s drop tower. The present tests involved gaseous fuel (either ethylene or propane), oxygen, and nitrogen. Various levels of nitrogen dilution were considered to obtain conditions where flames would ignite and then extinguish within the 2.2 s of available microgravity time.

Two modes of extinction onset were observed: base and hole extinction. Base extinction, typically observed at small flowrates, started at the base of the flame near the burner supply tube. Hole extinction, typically observed at high flowrates, started as a flame hole in the blue flame sheet at a distance away from the burner tube. Such holes grew with time. Base or hole extinction often led to complete extinction, where all blue-flame luminosity disappeared during a drop test. For flames in which base extinction was observed, extinction time is reported as the time when 50% of the previously visible flame surface (as viewed by the video camera) was no longer visible. For flames in which hole extinction was observed, extinction time is reported as the time when a hole was first visible. For some tests a resistively heated wire was placed around the burner tube and was energized (in microgravity) to help prevent base extinction.

Approximate relative peak temperatures were measured using thin-filament pyrometry, a technique pioneered by Villimpoc and Goss (1988). Four SiC fibers with diameters of 13.9 μm were strung across the flames in the focal plane of a Nikon D100 digital single-lens reflex camera. This color camera has 30(the still camera used by (Connelly with a shutter time of 33 ms. This d 2200 K using thermocouples in a measured temperatures have an est applied to determine peak gas tem flames, based on a fiber temperatur

Figure 1.10 illustrates base e without the heating wire. Extinctic cases, indicating that the time to burner supply tube. It was assumed

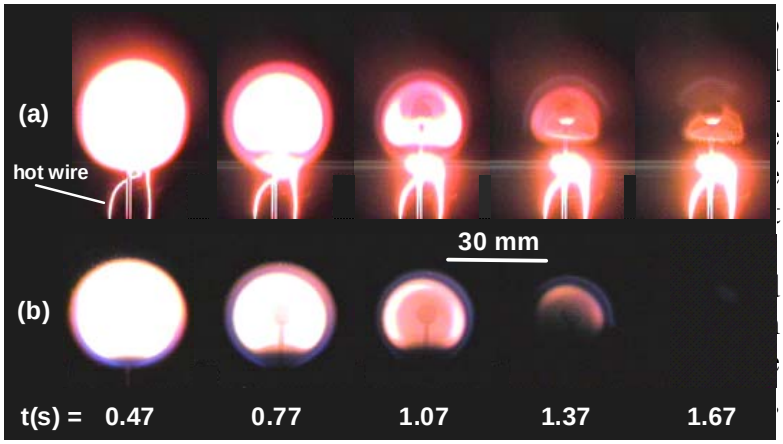

Figure 1.10. Time sequences of color images of extinguishing flames of propane flowing into air at 0.75 mg/s (a) with heating wire and (b) without. (Santa *et al.*, 2007a).

within the experimental uncertainties, and thus subsequent tests were performed without the heating wire.

Results for extinction time and extinction radius as a function of flowrate for propane flowing into 17% oxygen are shown in Fig. 1.11. Two extinction times are shown: base extinction and hole extinction. There is satisfactory agreement between experiment and computation for the extinction radius. Nonetheless, the numerical results for extinction time at low flowrates show a trend that does not agree with experiments. In Fig. 1.11, except for a narrow range of low flow rates, the extinction time predicted by the computations monotonically decreases and asymptotes to 2 s.

Although burner heat loss affects the time to extinction, it cannot trigger extinction for these flames because as the flame expands with time, heat loss decreases. Instead, extinction is triggered by radiative heat loss, which increases with time. For the lower flowrate cases, the enthalpy that is removed from the gas mixture due to burner heat loss causes radiative extinction to occur at shorter times.

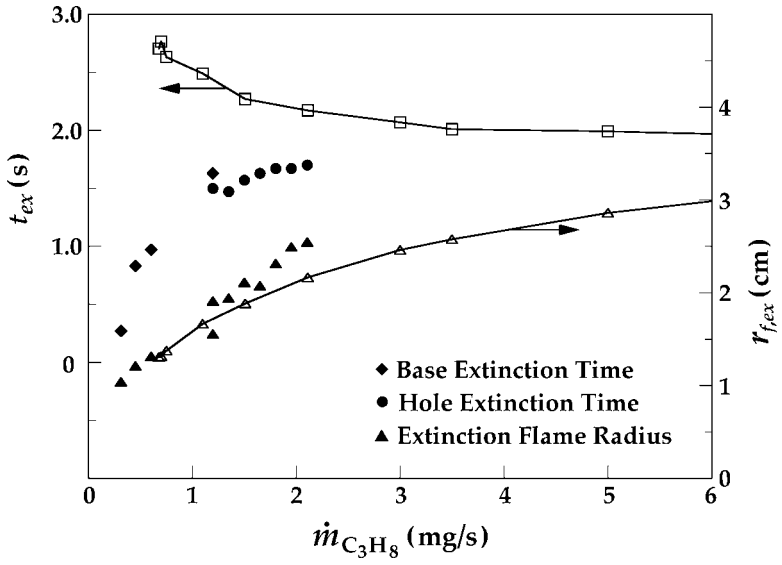

Figure 1.11. Measured and predicted extinction times and extinction radii for flames of propane flowing into 17% oxygen. (Santa *et al.*, 2007a).

Thin-filament pyrometry measurements are shown in Fig. 1.12 for oxygen flowing into 5% ethylene at various flowrates. Also shown are representative numerical predictions for oxygen flowing into 4% ethylene. The measurements were taken at a slightly higher ethylene concentration to retard filament-induced extinction. The measurements show that, at any given time, flows greater than 5 mg/s result in peak temperatures that are independent of flowrate, whereas for lower flowrates peak temperatures decrease with decreasing flowrate. This is consistent with the numerical predictions. The inability of the pyrometer to obtain temperatures at 1.9 mg/s after extinction is attributed to temperatures below the 800 K pyrometer threshold.

The present results indicate an extinction temperature of about 1100 K for the present flames. This is lower than past measurements of this property in normal-gravity flames (Quintiere 2006). For example, Williams (1981) indicates an extinction temperature of 1500 ± 50 K for hydrocarbon combustion in oxygen/nitrogen mixtures. Macek (1976) reports an extinction temperature of 1600 K for both diffusion and premixed flames. The significantly lower temperature at extinction reported here for microgravity diffusion flames is consistent with radiative extinction, as predicted by the analytical study of Chao *et al.* (1990).

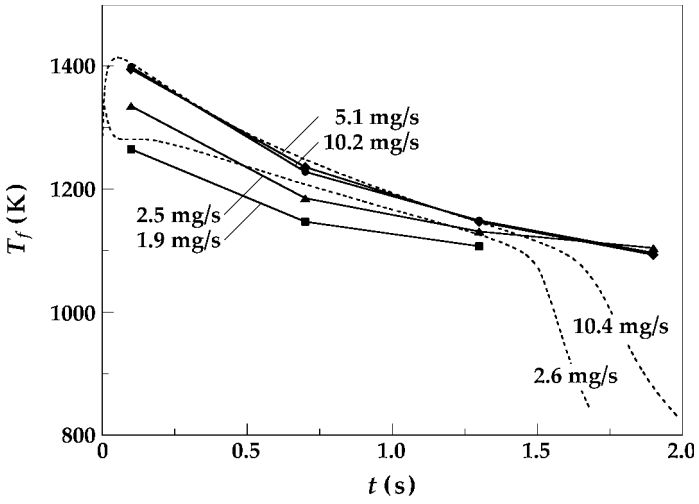

Figure 1.12. Pyrometer peak temperatures for flames of oxygen flowing into 5% ethylene (symbols). These are nonextinguishing flames except at 1.9 mg/s. Also shown are two representative numerical predictions for extinguishing flames of oxygen flowing into 4% ethylene (dashed curves). (Santa *et al.*, 2007a).

The major conclusions of this study were as follows. Radiative extinction was observed experimentally and numerically. Extinction time, peak temperature, and radiative loss fraction were found to be independent of flow rate except at very low flow rates. Radiative heat loss was dominated by the combustion product with flame surface area, not volume. For la with surface area and thus the radiative lo eak temperatures at extinction onset were a etic extinction. While radiative heat losses use radiative losses are increasing with tir flame expands away from the burner a

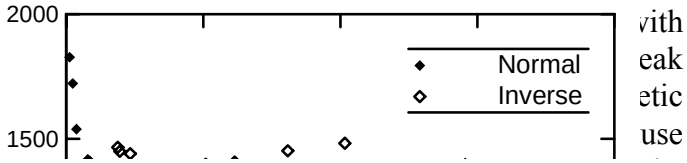

TABLE 1.2. Summary of the 17 experimentally identified sooting limit flames, (Lecoustre *et al.*, 2010)

Flame	Environment	$X_{C2H4,0}$	$X_{O2,0}$	Z_{st}	T_{ad} (K)	$\chi_{0.51}^{-1}$ (s)
1	Oxidizer	1	0.22	0.065	2390	14.56
2	Oxidizer	0.6	0.21	0.102	2326	7.09
3	Oxidizer	0.31	0.21	0.18	2226	2.74
4	Oxidizer	0.25	0.23	0.225	2238	1.72
5	Oxidizer	0.18	0.28	0.333	2306	0.86
6	Oxidizer	0.17	0.29	0.353	2308	0.78
7	Oxidizer	0.11	0.5	0.586	2381	0.37
8	Oxidizer	0.11	0.8	0.685	2528	0.23
9	Oxidizer	0.15	1	0.661	2740	0.12
10	Fuel	1	0.13	0.041	1847	10.16
11	Fuel	0.8	0.13	0.051	1835	8.08
12	Fuel	0.6	0.13	0.066	1814	6.14
13	Fuel	0.21	0.25	0.277	2274	1.95
14	Fuel	0.19	0.3	0.336	2370	1.88
15	Fuel	0.15	0.5	0.509	2539	2.34
16	Fuel	0.12	0.8	0.666	2578	4.55
17	Fuel	0.13	1	0.692	2670	5.09

Numerical Investigation of Spherical 2009)

This paper presents detailed numeric flames at their sooting limits. Sever considered (Sunderland *et al.*, 2004). but reached their sooting limits 2 s ranges of stoichiometric mixture fra 2670 K), and characteristic flow time transient diffusion flame code with losses from products were modeled u model coupled with a discrete-ordi examined, emphasizing profiles of dissipation rate.

A summary of the 17 sooting experiments were conducted to iden

yellow regions, but became all blue at 2 s after ignition (or slightly before). Burner flow rates were selected such that all flames involved a steady-state ethylene consumption rate of 1.51 mg/s, generating 71 W for complete combustion. Experiments were conducted with normal or inverse flames correspond to ambients containing either oxidizer or fuel, respectively. The fuel and oxygen mole fractions in the supply gases, $X_{C2H4,0}$ and $X_{O2,0}$, were varied widely, which yielded a wide range of Z_{st} as shown. Adiabatic flame temperatures reported in Table 1.2 were calculated using Chemical Equilibrium with Applications, CEA.

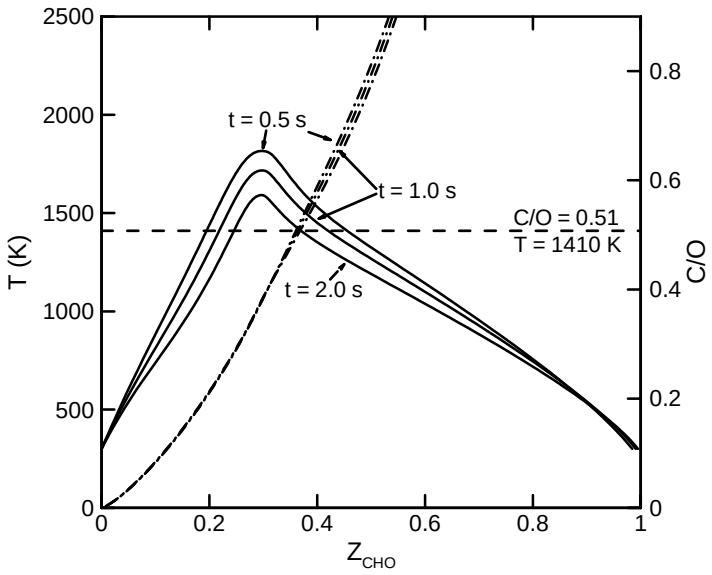

Figure 1.14. Temporal evolution of T (solid curves) and C/O (dash-dot curves) in Z space for flame 5. (Lecoustre *et al.*, 2010).

For sooting limit flames with sufficiently long flow times (i.e., above 0.5 s) a common observation observed for all flames, despite their disparate characteristics, was that soot does not exist unless there is a location in the flame where the C/O ratio exceeds 0.51 and the temperature exceeds 1410 K. As illustrated in Fig. 1.13, soot inception in flames with local flow times below 0.5 s required increased local temperatures or C/O ratios.

In Fig. 1.14, the temperature and C/O profiles in Z space for flame 5 at three times are considered to see if these findings can explain why the flames first appear yellow after ignition (i.e., are producing soot) and then become blue at 2 s. At times of 0.1 and 1.0 s, the experiments revealed abundant yellow emission from soot in the video record. This is supported by the computations, as Fig. 1.14 reveals regions where T > 1410 K and C/O > 0.51 at early times. In contrast, at 2 s the experiments reveal a sooting limit (i.e., they have transitioned to blue) and the computations predict the absence of any region with T > 1410 K and C/O > 0.51.

1.4 Normal Gravity Coflow Flame Research

Coflow flames in normal gravity can be strongly influenced by buoyancy because the gas velocities exiting the central tube are usually small compared to the velocities attained by the buoyant acceleration of the hot gases. Thus, unlike for the microgravity spherical flames, it is impossible to rigorously control convection direction. For example, in the normal flame, where fuel is ejected into oxidizer, one might expect the flow through the flame to be from fuel to oxidizer. This is not the case in the lower half of the flame, where the streamlines are from the oxidizer into the fuel owing to buoyant entrainment (Urban *et al.*, 1998). Sooting limits in normal gravity coflowing diffusion flames has been investigated by the PI in three recent journal papers (Kumfer *et al.*, 2006, 2008, Skeen, *et al.*, 2009).

While buoyant coflow flames suffer from ambiguities with respect to convection direction, they are simple to obtain, and with care information about the effects of structure and flow direction on sooting limits can be gleaned. In Kumfer *et al.* (2006) the criteria for soot inception in oxygen-enriched normal laminar coflow flames was explored. Methane, ethane, propane,

ethylene, and acetylene were used as fuels. The experimental apparatus included a coflow burner constructed with concentric tubes (with honeycomb) of diameters 8 mm (fuel) and 51 mm (oxidizer). The flames were overventilated, i.e., an increase in oxidizer flow rate did not affect the flame height or sooting limit. When possible, the inner and outer mass fluxes were held constant to minimize flow-induced strain. Flame heights were maintained at 16 ± 1 mm. Adiabatic flame temperatures were calculated using the CEA chemical equilibrium code (McBride and Gordon, 1996).

A cathetometer was used in a dim room to measure flame heights and to observe the sooting limit for each flame. Sooting limits were defined at a given axial height, measured from the flame base. The sooting limit was identified at which soot luminosity first appears at this predetermined height. The appearance of centerline soot occurred at much higher axial locations than that of near-flame soot. Sooting limits were obtained by varying the amount of nitrogen dilution.

Photographs of one-quarter, one-half, and three-quarters blue flames are shown in Fig. 1.15. The one-quarter, one-half, and three-quarter heights were 4, 8, and 12 mm, respectively, and the sooting limits were not a function of small changes in total flame height.

The sooting limit results for one-half blue ethylene flames are plotted in Fig. 1.16. For a given flame type, e.g., half blue, the adiabatic flame temperature at the sooting limit increased with Z_{st} by about 600 K. These trends are in agreement with previously published sooting limit results for propane coflow flames (Kang *et al.*, 1997), as well as for ethylene counterflow and spherical flames (Sunderland *et al.*, 2004). The results show good agreement between the two flame geometries, despite the added complexities associated with the coflow flames.

The major findings of this work can be summarized as follows. The sooting limit flame temperature was found to increase linearly with stoichiometric mixture fraction, regardless of fuel type. The local C/O atom ratio is a controlling parameter for soot inception in diffusion flames. Soot inception can occur only when the local C/O ratio is above a critical value. The values for critical C/O ratios obtained from the analysis of

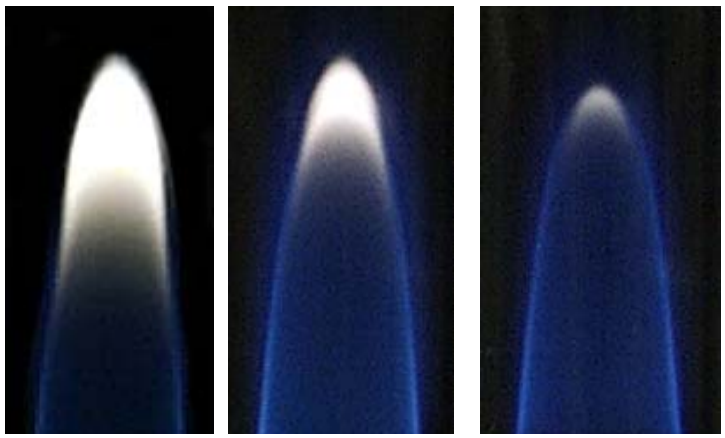

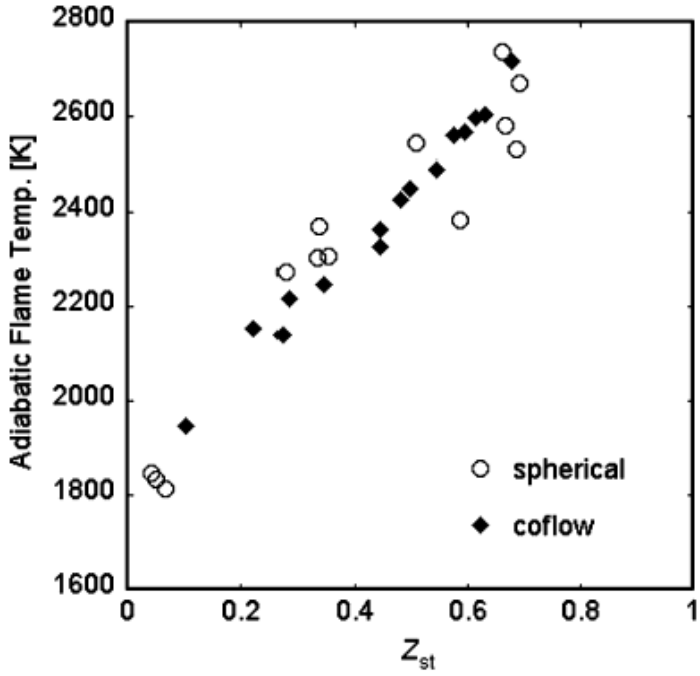

Figure 1.16. Comparison between the sooting limits of ethylene spherical diffusion flames and the present half-blue coflow flames. (Kumfer *et al.*, 2006).

experiments using several fuels are similar in magnitude to the corresponding C/O ratios for premixed flames. Temperatures and PAH fluorescence were measured to identify regions in these flames most conducive to particle inception. Results indicate that the peak PAH concentration lies along a critical contour of constant C/O, which supports our theory that soot particles first appear along this critical contour, given sufficient temperature.

2 FLIGHT EXPERIMENT

2.1 Knowledge Lacking and Knowledge to be Gained by Flight Tests

In addition to the fundamental data that will be obtained from the proposed experiments, there is considerable new understanding that will be gained. In particular, the controlling mechanisms for soot inception in nonpremixed flames will be elucidated, with emphasis on understanding how the structure of a nonpremixed flame can be tailored to yield a desired sooting characteristic for a given fuel. In addition, the effects of flame structure on flame extinction will be clarified, with emphasis on determining ways in which the structure can be affected to yield strong, robust low-temperature flames.

An important aspect of this work is that the parameters employed to characterize the laminar nonpremixed flames will be Z_{st} and the amount of inert in the flame (or, equivalently, T_{ad}). These two parameters characterize the basic structure of the flame and thus have a first-order effect on flame phenomena such as extinction and soot inception. In some respects they are analogous to equivalence ratio and amount of dilution for premixed flames. For example, in studying the soot limits of premixed flames, Glassman and Takahashi (1984) varied equivalence ratio and T_{ad}. Their work identified competition between formation and oxidation reactions as the controlling feature responsible for the onset of soot in premixed flames. In the present study of nonpremixed flames, Z_{st} also affects precursor formation and oxidation reactions but from a *structural* perspective, not a kinetic perspective. This is effectively why we believe high Z_{st} flames do not soot. Soot precursor oxidation on the fuel side of diffusion flames (not to be confused with soot oxidation that occurs when soot passes into the oxidizer side, for example, in a coflow flame) is generally considered to be negligible. However, this is only the case at low Z_{st}. Thus the findings of this work will open up a new understanding of soot formation in nonpremixed flames. These findings will also have practical value because as pollution control becomes more stringent and oxygen separation technologies become cheaper, burning at oxygen-enriched air conditions (high Z_{st}) will become more prevalent.

Just as there is a loose analogy between equivalence ratio in premixed flames and Z_{st} in nonpremixed flames for soot formation, there may be a similar analogy vis-à-vis flammability limits. Flammability limits are fundamental limits of flame propagation in premixed flames and are generally described in terms of equivalence ratio. The primary factors influencing these limits are the rates of heat generation and heat loss. When heat loss becomes comparable to heat generation, the temperature becomes too low to generate a sufficient radical pool and the flame will not propagate. As we have shown for nonpremixed flames the radical pool is also affected by Z_{st} and there is a unique value of Z_{st} at which the temperature reaches a minimum before extinction. Identifying this value of Z_{st} in one-dimensional flames, where the only heat loss is the intrinsic radiative heat loss of the flame, will yield a limit that is analogous to a flammability limit – thus the term pseudo-flammability limit. Just as the flammability limits of premixtures represents an important practical limit as it represents conditions where a given mixture can burn, the pseudo-flammability limit represents the limiting condition where a nonpremixed flame can exist for a given fuel burning with an inert and oxygen.

2.2 Experimental Objectives

Thus motivated, the primary objectives of this flight experiment are listed here in priority order:

A. Obtain soot-inception limits of quasi-steady normal and inverse spherical diffusion flames as functions of flow rate, Z_{st}, amount of inert (N_2 or CO_2[**]), and pressure[**] for C_2H_4 and CH_4[*] flames. Identify the corresponding temperatures in hot regions. Obtain similar limits and temperatures for inverse and normal coflow flames[**].

B. Obtain detailed measurements in quasi-steady normal and inverse spherical diffusion flames for C_2H_4 and CH_4[*]. Determine the effects of flow rate, Z_{st}, amount of inert (N_2 or CO_2[**]), and pressure[**] on flame temperature, size, color, and soot volume fraction. Evaluate the possible existence of steady flames. Obtain similar measurements for inverse and normal coflow flames[**].

C. Obtain extinction limits as functions of Z_{st}, amount of inert (N_2 or CO_2[**]), and pressure[**] for normal and inverse spherical C_2H_4 and CH_4[*] flames. Identify the corresponding temperatures in hot regions. Identify the presence of radiative or kinetic extinction. Evaluate whether pseudo-flammability limits can be obtained for these flames. Measure blowoff limits for inverse and normal coflow flames[**].

[*]desired; [**]highly desired.

2.3 Summary of Approach

This study emphasizes spherical diffusion flames. The reaction zone rests near the porous sphere and a large thermal field surrounds the flame. Since the flame is effectively one-dimensional, diagnostics along one radial line are sufficient to characterize the flame.

Unfortunately, the maximum permissible oxygen mole fraction in the chamber is 50%, which limits the range of Z_{st} that can be obtained. Consequently, microgravity coflow flames are proposed because they allow for higher oxygen concentrations and for comparison with normal gravity results of the PI (Kumfer *et al*., 2006, 2008, Skeen *et al.*, 2009). While coflow flames are two dimensional, they can be used in the ACME (2010) facility to obtain inverse flames by supplying oxidizer to the central jet and fuel to the outer stream. Furthermore, higher oxygen concentrations can be achieved because the combustion chamber (initially filled with nitrogen) will not encounter high oxygen concentrations. The coflow geometry adds complexity to the interpretations, but it has advantages over the spherical flame in that it is easier to change operating conditions and quicker to reach steady state. Thus the coflow flames will compliment the spherical flame studies and are considered an integral part of this study. Nonetheless, the ability to directly compare normal and inverse coflow flames would be of greater value than comparing inverse coflow flame results and normal spherical flame results.

To accomplish the objectives, the flames must be characterized in terms of the existence of a flame (to identify the extinction limit), flame location, temperature field, the onset of soot (soot-inception limit) and, where applicable, the soot field. In addition, a number of preliminary measurements must be performed to ensure that the results are accurate and precise. For example, measurements will be performed to ensure the flames have approached quasi-steady state and that, in the case of spherical flames, that the flow rate from the porous sphere is sufficient to minimize heat loss to the sphere.

The soot-inception limits of spherical flames will be obtained by observing flames that grow with time. As they grow, their radiative losses increase and their peak temperatures

decrease. For the present test matrix it is estimated that sooting limits will be observed within 10 - 30 s of ignition.

Radiative extinction will be obtained by observing flames that grow in size with time until extinction (Santa *et al.*, 2007a). With terrestrial flames, the lack of a visible luminous flame has been assumed to indicate extinction. Nonetheless, microgravity flames can be significantly weaker than normal gravity flames, and Tse *et al.* (2001) have raised concerns that the CH emission may not be sufficient to detect the existence of a flame at the low temperatures at which microgravity flames extinguish. In other words, a flame may exist even though there is no discernable flame emission. To address this concern, the following procedure will be adopted: after the flame emission sensor(s) indicate extinction has occurred, the flow rate will be reduced to confirm extinction. If the flame has not extinguished, it is expected to reappear.

It is anticipated that the temperature field will be measured with a combination of two-color pyrometry from soot (Urban *et al.*, 1998) and thin-filament pyrometry (Maun *et al.*, 2007). Far field temperatures will be measured with thermocouples. Where applicable, soot volume fraction will be measured with laser extinction.

Comprehensive numerical modeling, including detailed chemistry, transport, and radiative heat loss from the gas phase and burner surface (Santa *et al.*, 2007a, 2007b), will support the operation of the experiments and will contribute significantly to understanding and interpreting results. Key experiments will be simulated numerically to ensure that the operating conditions selected are optimum and that the diagnostics are appropriately chosen (e.g., camera field of view) to obtain the desired results. As the detailed flame structure is fundamental to this work and it will not be possible to obtain concentration profiles, it is essential that major and intermediate species be modeled with good accuracy. The PI team has published two journal papers with results of their computational model for spherical diffusion flames (Santa *et al.*, 2007a, 2007b). The PI team also has access to computational models that are suitable for analyzing the present coflow flames.

The PI team's spherical flame model computes the transient and steady state solutions of spherically-symmetric diffusion flames (Santa *et al.*, 2007a, 2007b). The code includes a sectional model to simulate particle dynamics and, if needed, this can be used to model soot particle growth. Nonetheless, the primary goals of this research involve soot-inception limits, not soot formation, and thus it should be possible to accomplish the objectives by considering only gas phase species, as has been done for premixed flames (Markatou *et al.*, 1993).

Initially this model was used with the GRI-Mech 3.0 mechanism. However a mechanism with larger hydrocarbons has been implemented (Lecoustre *et al.*, 2009). Soot-precursor species up to pyrene are included. A number of mechanisms have been proposed (Markatou *et al.*, 1993, Smooke *et al.*, 1999) and the sooting limit data will be a critical test of the accuracy of the mechanisms in predicting soot inception.

2.4 Science Data End Products

Having defined the objectives of this investigation, it is now possible to define a group of final data products that is sufficient to fulfill each objective. Final data products are the tables, figures, and analyses that will be reported in the archival literature (not the raw data from the experiment). These final data products are referred to as the "Science Data End Products" (SDEP). To facilitate comparison of the planned SDEP with the objectives, they are summarized in Table 2.1. The science requirements and the experiment success criteria described below are developed from this list of SDEP.

Table 2.1. Objectives and science data end products.

	Objectives	Science Data End Products
A.	Obtain soot-inception limits of quasi-steady normal and inverse spherical diffusion flames as functions of flow rate, Z_{st}, amount of inert (N_2 or CO_2**), and pressure** for C_2H_4 and CH_4* flames. Identify the corresponding temperatures in hot regions. Obtain similar limits and temperatures for inverse and normal coflow flames**.	A1 Color images A2 Temperature profiles A3 Temporal plots of flame diameter (shape) and temperature A4 Plots of soot-inception limits
B.	Obtain detailed measurements in quasi-steady normal and inverse spherical diffusion flames for C_2H_4 and CH_4*. Determine the effects of flow rate, Z_{st}, amount of inert (N_2 or CO_2**), and pressure** on flame temperature, size, color, and soot volume fraction. Evaluate the possible existence of steady flames. Obtain similar measurements for inverse and normal coflow flames**.	B1 Color images B2 Temperature profiles B3 Temporal plots of flame diameter (shape) and temperature B4 Soot volume fraction profiles B5 Plots of $f_{s,\max}$, T_f, and soot-inception limits as functions of flow rate B6 Quasi-steady flame diameter (shape) as a function of Z_{st} and flow rate B7 Plots of flame diameter (shape) versus time
C	Obtain extinction limits as functions of Z_{st}, amount of inert (N_2 or CO_2**), and pressure** for normal and inverse spherical C_2H_4 and CH_4* flames. Identify the corresponding temperatures in hot regions. Identify the presence of radiative or kinetic extinction. Evaluate whether pseudo-flammability limits can be obtained for these flames. Measure blowoff limits for inverse and normal coflow flames**.	C1 Color images C2 Temperature profiles C3 Temporal plots of flame diameter and temperature C4 Plots of extinction limits C5 Effects of flowrate on extinction limits and T_f

* denotes desired; ** denotes highly desired.

2.5 Justification for Extended-Duration Microgravity

Previous ground-based microgravity experiments have demonstrated the value of the spherical, burner-supported nonpremixed flames for flame studies. The one-dimensional flame offers a simple, fundamental configuration to improve our understanding of nonpremixed flame behavior and to explore such effects as radiation and thermophoresis, which are more pronounced under microgravity conditions (Atreya *et al.*, 1992, Law *et al.*, 2001). The burner-supported spherical flame is in some respects similar to droplet burning but it holds the advantages that larger flames are possible and, with sufficiently long time, can approach quasi-steady state. Furthermore, the proposed microgravity coflow flames allow the direction of convection across the flame to be varied.

Although the spherically-symmetric flame geometry has many advantages, it is not practical to produce such a flame at normal gravity. The reason for this can be understood by considering the Richardson number, *Ri*, which is the ratio of the buoyancy force to the inertial force and is given by

$$Ri = \left(g \frac{\Delta T L}{T u^2} \right) . \tag{2.1}$$

Here g is the acceleration of gravity, T is temperature, L is the characteristic length scale, and u is the characteristic velocity. Taking L as the burner diameter, u as the ejection velocity at the

burner surface, and $\Delta T = (T_{ad} - T_b)$, we find that Ri is on the order of 1000 in normal gravity. In fact, it is much higher than this because the more appropriate length and velocity scales are the flame diameter and the velocity at the flame, respectively. The value of Ri can be reduced by judicious choice of fuels and inert; Law *et al.* (2001) have shown that nearly spherical flames can be created in normal gravity. However, Ri for these flames is still on the order of unity, implying that while the flames appear spherical, natural convection is still present. Furthermore, hydrogen must be used as a fuel and be supplied in the ambient so such flames are not relevant to this study. A reduction in Ri can be achieved by reducing the flame size, but substantial reduction in L is not practical because our goal is to produce a flame that is sufficiently large that its structure can be characterized. Furthermore, heat loss to the burner would be excessive for small flames. Consequently, for general fuels and inerts the only practical method of obtaining $Ri << 1$ is to reduce g by four orders of magnitude. This can be accomplished in a number of microgravity environments, including ground-based facilities, e.g., drop towers for short times, as well as flight experiments, e.g., the International Space Station for longer times. A quantitative evaluation of the acceptable g levels for these experiments is given in Appendix A and is discussed below.

The drop-tower results detailed in Section 1.3 have demonstrated the value of the spherically-symmetric burner stabilized flame. The ability to reverse flow direction has helped to elucidate the dominant mechanism responsible for permanently-blue flames, yet the results are not conclusive because transient effects could dominate these observations. Transient effects arise from two sources: the ignition process and the long times required for spherical microgravity flames to reach quasi-steady state. The ignition process is not spherically symmetric and thus there is an asymmetry imposed by ignition that must be damped out. More importantly, soot particles that are created during ignition can be trapped in the interior of the flame due to thermophoresis. The particles are trapped for the same reasons that a soot shell is produced in microgravity droplet combustion (Choi *et al.*, 1991, Avedisian and Callahan, 2000). Thus, it is possible for soot to exist in flames after the ignition event even though the flame has ceased producing soot.

The reason the spherically-symmetric burner-stabilized flame takes so long to reach quasi-steady state is that the radial velocity scales with $1/r^2$. Thus, at only a few burner diameters away from the sphere, diffusion is the dominant mechanism of transport. Since the characteristic diffusion time τ_d is given by r^2/D, τ_d is on the order of tens of seconds a few centimeters from the burner. Decreasing the flame size will decrease the size of the thermal field and, consequently, the time to reach quasi-steady state, but there are limits to the minimum flame size that is possible. These limits are imposed by the need to avoid heat loss to the burner and ensure flame sphericity. Experiments performed in the 5 s drop facility indicate that for many of the run conditions needed for the proposed experiments the flame is still growing significantly after 5 s. Analytical (see Appendix A) and numerical calculations predict that up to 30 s of jitter-free (less than 10^{-5} g) microgravity is needed to approach quasi-steady state for these run conditions. No ground-based facilities are available to accomplish this.

In some ways, the spherical flame experiments are the nonpremixed analog to premixed flame balls because in both systems diffusion dominates the development of the far field temperature distribution. Therefore, this work is subject to the same needs as SOFBALL (Ronney *et al.*, 1998) in that long duration microgravity is needed and g-jitter must be negligible because the thermal field is very large and convection is small, i.e., Ri is large even for small g.

To provide a quantitative assessment of the acceptable gravity level, an analysis was performed, as detailed in Appendix A. In this analysis, the acceleration induced on a fluid packet by natural convection is formulated by considering a gravitational acceleration given by a sinusoidal function. The resulting acceleration function for the fluid packet is next integrated to obtain the gravity induced flow velocity. This velocity can be converted to an additional mass flux that transports the flame front and causes distortion of the flame. By specifying the maximum percentage of distortion allowed in the experiment (10% here), the acceptable gravity level is determined, and this result is given in Fig. 2.1 for the four flames of Table 1.1. As shown, the required g levels are on the order of 10 μg. This is too for microgravity aircraft, but is consistent with the anticipated environment of the Combustion Integrated Rack (CIR). Finally, it is important to emphasize that the proposed experiments illustrate an important and novel use of microgravity for combustion research. In microgravity we are able to hold Z_{st} fixed and in coflow tests vary the direction of convection through the flame. There are no analogous experiments at 1g that can accomplish this.

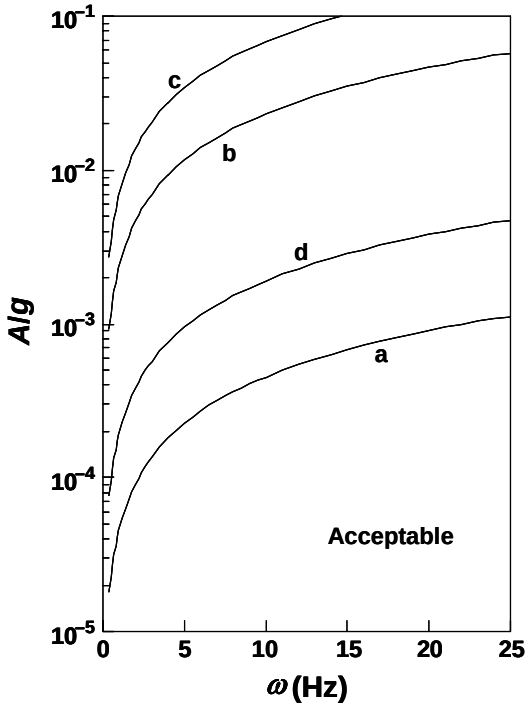

Figure 2.1. Allowable g-levels as a function of frequency for the four flames (a) – (d) described in Table 1.1. A/g is the acceleration nondimensionalized with respect to normal gravity.

Experiments have been performed in normal gravity coflow flames to understand the effects of flame structure and flow direction on soot formation (Kumfer *et al*., 2006, 2008, Skeen *et al.*, 2009). As mentioned previously, owing to the effects of buoyancy on the flow field, the flow direction cannot be prescribed in normal gravity coflow flames as it can in microgravity spherical flames or microgravity coflow flames. For example, it is well known that for fuel issuing into an ambient of air, buoyancy accelerates the flow field and causes the streamlines to be from oxidizer to fuel in the lower regions of the flame and from fuel to oxidizer in the upper regions (Santoro *et al.*, 1987). The importance of buoyancy to the flow field will vary with Z_{st} because the velocity and thus Ri are strongly affected by dilution. In other words, the relative amount of entrainment will vary with Z_{st} in buoyant flames. Thus, normal gravity flames have ambiguities with respect to flow direction as Z_{st} is varied. Nonetheless, coflow flames have been valuable in confirming the role of Z_{st} on flame structure and the effects of residence time on soot inception (Kumfer *et al.*, 2006, 2008, Skeen *et al.*, 2009).

Microgravity gas jet flames in quiescent surroundings have been observed in drop towers and the Space Shuttle and the results have revealed significant differences between the two in terms of sooting behavior, suggesting that the drop tower results were far from steady state (Urban *et al.*, 1998). Velocities in coflow flames are similar to those in gas jet flames in quiescent environments. Therefore the impact of buoyancy on coflow flames is expected to have a similar impact to that reported in Urban *et al.* (1998). Thus, drop tower coflow experiments are not a viable option for studying quasi-steady microgravity coflow flames. The characteristic

times in these flames are long and thus the scalar fields develop much slower that in normal gravity, indicating that long duration microgravity is needed.

3 EXPERIMENT REQUIREMENTS

3.1 Requirements Discussion

The Flame Design experiment requirements are included in the ACME (2010) Science Requirements. This discussion below provides background on many of these requirements and relates them to the experiment objectives.

Spherical Burner

The science return of this experiment is predicated on the ability to produce nearly 1-D spherical flames. Significant deviation from flame sphericity could invalidate our comparisons with analytical and numerical models because those models assume one-dimensional flames.

Testing in the 2.2 s drop tower has demonstrated the high impact of burner design on flame sphericity. These tests also have demonstrated the value of the parameter r_{min}/r_{max} in quantifying flame sphericity. The ACME (2010) requirements were derived from an analysis of the effects of nonsphericity.

In addition to sphericity, the burner must be able to survive high temperatures. Tests that produce excessively hot burners will be avoided owing to fuel pyrolysis and excessive radiative loss. Pyrolysis testing within a furnace and considerations of radiative emissions led to the guideline that burner temperature should not exceed 450 ºC. This places an upper limit on burner size and a lower limit on flame size. The PI team will seek operating conditions such that the burner reaches 95% of quasi-steady-state temperature for all flames considered within 30 s.

The requirement for sphericity is most easily met by increasing burner diameter, while that of minimizing burner heating is met by decreasing burner diameter. Ground-based testing and numerical analysis indicate that a sphere of 6.4 mm in diameter is a good compromise (see Figs. 1.5, 1.6, and 1.10). The feed tube has been found to be critical, both in terms of its disturbance to the flame and its seal with the porous sphere. Dimensions, materials and method of attachment to sphere are critical to maximizing sphericity and minimizing disturbance to the flame.

Coflow Burner

Flame Design has no requirements for the coflow burner other than those specified by the CLD Flame team.

Burner Gas Delivery

The science return of this experiment depends on the ability to control the composition and flow rate of the spherical burner gas and the coflow gas streams. Requirements in this section generally were established by modeling and observations of spherical flames in the NSA Glenn 2.2 and 5 s drop facilities.

Ignition

Ignition disturbances should be minimized to allow comparison with the numerical model and with observations in the NASA 2.2 and 5 s drop facilities.

Ambient Environment

The science return of this experiment depends on the ability to control the ambient environment prior to each combustion test. The chamber contents initially must be isothermal and quiescent. Flow rates and chamber volume may be limited by the requirement for burn-time variations in ambient composition, temperature and pressure. Suggested methods to decrease bottled gas consumption rates include partial venting and filling, and scrubbing for CO_2 and H_2O. Tests with coflow flames will involve a chamber initially filled with N_2.

Monitoring Measurements Requirements

To ensure repeatability, evaluation of the approach to quasi-steady-state conditions, and to provide reference data for the model predictions, these measurements are required. All of these measurements must be initiated before test operations begin and continue sufficiently past the flame extinction to allow a baseline measurement. Monitoring of the fluent flow rates and temperatures are required. Ambient condition measurements (pressure and temperature) are also required (while oxygen concentration measurement is desired), as model results have shown the flames are sensitive to these parameters.

Color Imaging

Color imaging will be used to determine flame size, shape, color, and sooting limits. In addition, it will provide confirmation of other diagnostics used for detecting extinction limits. Flame size will be needed to verify proper operation and to validate numerical models. Flame shape will be used to measure r_{min}/r_{max}.

Identification of conditions that lead to the onset of soot particle formation, i.e., the sooting limit, is a critical requirement. Ground based-studies have shown that the onset of visible yellow luminosity is a good indicator of the onset of particles for normal gravity flames (Du *et al.*, 1988). The basis for the correlation between the yellow luminosity and the onset of soot is that soot inception occurs in regions of sufficiently high temperature that yellow emission will occur. Nonetheless, the characteristics of the proposed experiments are such that flow direction can force particles into cooler regions and residence times are much longer than in normal gravity flames. Thus, the assumption that the onset of visible yellow luminosity can be used to identify the soot inception limit for a given run condition will need to be supported by measurements that are not dependent on local temperature.

Visibly luminous soot will be observed with color cameras. Because flames can be asymmetric, a second view would minimize ambiguity. The field of view will need to be sufficiently large to observe the entire flame while at the same time be sufficiently small to allow for resolution of the fine scale needed to identify the onset of soot inception. For this reason, zooming capability is desired. When yellow luminosity is just barely detectable, this condition is defined as the soot-inception limit.

Temperature

Accurate measurement of gas temperature distributions is essential to this work. Flame temperature and temperature distribution are affected by flowrate, Z_{st} and flow direction, and temperature measurements are required to understand the effects of these parameters on soot formation and flame extinction. Furthermore, peak temperatures at the soot inception limit and near the flame extinction limit are required. These limit temperatures are particularly important because the premise is that flame structure (Z_{st}), can dramatically affect limit temperatures. For

example, as described above, judicious variation in Z_{st} should lead to a minimum extinction temperature that is hundreds of Kelvins lower than that of standard Z_{st} flames (hydrocarbon burning in air). Also, soot inception is affected by Z_{st} because the temperature distribution and concentration distribution are shifted relative to each other. Thus, a spatially accurate temperature profile is necessary to validate this theory.

Microgravity spherical diffusion flames occur in weakly convective fields such that the flames are particularly prone to disturbance by intrusive probes (e.g., thermocouples). In addition, near the extinction limits, heat or radical loss to an intrusive probe can extinguish the flame. Nevertheless, thermocouple probes are accurate and are requested here for the purpose of validating the other temperature diagnostics. These probes may be removed for tests after this validation is complete.

Temperature will be measured in such a way that radial temperature profiles can be obtained within the specifications given. The rationale for these specifications is based on the need to sufficiently resolve the anticipated features of the temperature distribution, e.g., peak temperature and location, and to observe temporal variations. The temperature distribution for these flames is anticipated to be much broader than for normal-gravity flames. Thus it is required to measure temperatures from close to the burner to the cool region on the ambient side of the flame. For spherical flame tests, there must be a measurement of burner surface temperature at a location sufficiently far from the burner feed tube.

Soot Volume Fraction

To determine the dominant mechanism responsible for permanently-blue flames, a measure of the distribution of soot volume fraction is required. This information will identify the inception zones and surface growth zones in soot-bearing flames. Soot volume fraction will be measured with laser extinction and deconvolution. This method has been used successfully by other flight experiments and in ground-based work by the Flame Design investigators.

Radiant and Chemiluminscent Emissions

Flame extinction will be inferred by photomultiplier tubes and imaging. To ensure that extinction has occurred, flow rate will be reduced to a condition for which a stable flame had previously been observed. If the flame does not reappear, it can be assumed that the flame had extinguished.

UV emission will also be used to indicate the presence of a flame. While it is generally believed that the existence of a hydrocarbon flame can be detected by observation of blue emission, this may not be the case with microgravity flames because these flames are extremely weak and we are attempting to produce the lowest temperature diffusion flames that have been produced. SOFBALL experiments (Ronney *et al.*, 1998) demonstrated that a UV camera has sufficient sensitivity to detect flame balls, which should be of equivalent strength to our weakest flames. Thus, measurement of broad-field UV emission should indicate the presence of a weak flame.

Just as the flammability limit in premixed flames is a fundamental limit representing conditions where the flame transitions from non-flammable to flammable, we believe there is an analogous limit for diffusion flames. This limit is referred to as the pseudo-flammability limit. Whereas in premixed flames the flammability limit is a function of the fuel-type, oxidizer (i.e., the amount of inert) and equivalence ratio, in nonpremixed flames we expect it to be a function of fuel-type, amount of inert and Z_{st}. By measuring flame extinction under conditions specified in the test matrix, the pseudo-flammability limit can be inferred.

3.2 Operational Sequences
The Flame Design operational sequences are summarized in ACME (2010).

3.3 Test Matrix
A detailed test matrix is given in ACME (2010). A brief discussion is provided below.

Spherical Flames
These tests will emphasize measurements of three types of limits: sooting limits, radiative extinction limits, and kinetic extinction limits. Tests will involve normal and inverse convection directions. A smaller number of tests will consider long-term burns to evaluate the possible existence of steady flames. These tests support Objectives A – C.

Coflow Flames
These tests will emphasize inverse coflow flames (highly desired), and flames with high oxygen concentrations in the oxidizer. Measurements will emphasize sooting limits, defined here as half-blue limits. A half-blue soot limit is a condition where the lowest visible yellow emissions are half way between the burner tip and the visible flame tip. These tests support Objectives A and C.

3.4 Science Success Criteria
The success of the proposed experiment will be judged vis-à-vis the stated objectives. The requirements for four levels of success are stated.

Minimal success requires:
Obtain color images of a spherical flame of C_2H_4 flowing into diluted oxygen that passes its sooting limit, passes its radiative extinction limit, and has a total burn time that exceeds 20 s.

Obtain color images of a spherical flame of C_2H_4 flowing into air as a function of m.

Substantial success additionally requires:
Measure peak temperature as a function of m for a spherical flame of C_2H_4 flowing into diluted oxygen at quasi-steady conditions.

Obtain soot inception limits and extinction limits for spherical C_2H_4 flames as functions of Z_{st} and T_{ad}.

Complete success (which requires completion of the required test matrix) additionally requires:
Perform tests S1 – 47 or a similar set of spherical flame tests.

Obtain temperature distributions at (or near) the sooting and extinction limits of spherical flames.

Measure soot volume fraction profiles for spherical diffusion flames at low and high Z_{st}.

Superior success (which includes only desired items) additionally requires:
Obtain color images of inverse coflow flames of diluted oxygen flowing into C_2H_4 at quasi-steady conditions as a function of m.

Obtain soot inception limits and extinction limits for inverse coflow flames of diluted oxygen flowing into C_2H_4 as functions of Z_{st} and T_{ad}.

Obtain soot inception limits and extinction limits with CO_2 diluent as functions of Z_{st} and T_{ad} for normal spherical and (coflow) inverse flames.

Obtain soot inception limits and extinction limits for C_2H_4 as functions of Z_{st} and T_{ad} for normal and (coflow) inverse flames at pressures of 0.2 and 0.5 atm.

Obtain soot inception limits and extinction limits for CH_4 as functions of Z_{st} and T_{ad} for normal spherical and (coflow) inverse flames.

3.5 Post Flight Data Analysis Plan

The bulk of the test matrix for this investigation is intended to determine the soot-inception and flame-extinction limits as a function of Z_{st} and T_{ad}. The efficient use of consumables in this investigation will allow us to examine the limits for a large number of flames. Due to the fact that the conditions leading to the soot-inception and extinction limits are unknown, we will be acquiring extensive image data. The bulk of our analysis will focus on the flame status near the limits, although a number of flames will be studied under more robust conditions to ensure the effectiveness of the model predictions of flame size and temperature.

Much of the post-flight data analysis will occur in the course of mission operations as the science team evaluates each set of test runs in preparation for subsequent runs. The initial tests with spherical flames are designed to uncover the effects of burner heating, chamber wall effects, flame size and flame radiation on the experimental results. These tests will also be used to establish an initial understanding of the soot inception and extinction limit plots. Consequently, these tests will receive substantially more scrutiny than many of the subsequent tests. Analysis of these tests will include: tracking of flame size and concentricity as a function of time for each test; analysis of discrete signals (e.g., radiometers, photomultipliers, and pressure transducers) for evidence of the quasi-steadiness of the flames; analysis of the temperature profiles (thin filament, soot temperature, and far-field thermocouples) to ensure agreement with the models and to evaluate quasi-steadiness; and deconvolution of soot volume fraction measurements to evaluate the effect of flame size on the soot volume fraction.

For subsequent tests, the operating conditions at the soot-inception and extinction limits will be tabulated and plotted with Z_{st}, T_{ad}, and T_{ext}. Flame temperatures near extinction will be determined either by deconvolution of the soot temperature data or by thin fiber pyrometry. Periodic deconvolution of the soot volume fraction data will be performed to allow evaluation of the effect of flow inversion and flame structure. The deconvolution and fiber pyrometry data will be analyzed primarily near the inception and extinction limits.

4 REFERENCES

ACME-SRD-001, Advanced Combustion via Microgravity Experiments, Science Requirements, NASA Glenn Research Center (2010).

Assanis, D.N., Karvounis, E., Sekar, R.R. and Marr, W.W. (1993) ASME Journal of Engineering for Gas Turbines and Power, Vol. 115, pp. 761-768.

Atreya, A. and Agrawal, S. (1998) *Combust. Flame* 115:372-383.

Atreya, A., Wichman, I, Guenther, M. Ray, A. and Agrawal, S. (1992) "An Experimental and Theoretical Study of Radiation Extinction of Diffusion Flames," Second International Microgravity Combustion Workshop, NASA Lewis Research Center, Cleveland, OH, Sept. 15-17.

Avedisian, C.T. and Callahan, B.J. (2000) *Proc. Combust. Inst.* 28(Pt. 1), 991-997.

Baukal, C.E. (Ed) (1998) Oxygen Enrichment Enhances Combustion, CRC Press.

Batchelor, G. K. An Introduction to Fluid Dynamics. Cambridge University Press, Cambridge, 1983, p.454.
Callaghan, K., Nemser, S., Poola, R.B., Stork, K.C., Sekar, R.R. and Johnson, B. (1998) SAE Paper 980177.
Chace, A.S., Hazard, H.R., Levy, A. Thekdi, A.C. and Ungar, E.W. (1989) Combustion Research Opportunities for Industrial Applications – Phase II, U.S. Department of Energy report DOE/ID-10204-2, Washington, D.C.
Chao, B.H., Law, C.K. and T'ien, J.S. (1990) *Proc. Combust. Inst.* 23, 523-531.
Chao, B.H., Liu, S. and Axelbaum, R.L. (1998) *Comb. Sci. Tech.* 138:105-135.
Chen, R. and Axelbaum, R.L. (2005) *Combust. Flame* 142:62-71.
Choi, M.Y., Dryer, F.L. and Haggard, J.B. Jr. (1991) *Proc. Combust. Inst.* 23 1597-604.
Connelly, B.C., Kaiser, S.A., Smooke, M.D. and Long, M.B. (2005) Fourth Joint Meeting of the U.S. Sections of the Combustion Institute, Philadelphia.
DeLombard, R. Compendium of Information for Interpreting the Microgravity Environment of the Orbiter Spacecraft. NASA Technical Memorandum 107032, 1996.
Dietrich, D.L., Haggard, J.B., Dryer, F.L., Nayagam, V., Shaw, B.D. and Williams, F.A. (1996) *Proc. Combust. Inst.* 26, 1201-1207.
Doctor, R.D., Molburg, J.C. and Thimmapuram, P.R., (1997) *Energy Conv. and Mgmt.*, 38:575-580.
Du, D.X., Axelbaum, R.L. and Law, C.K. (1988) *Proc. Combust. Inst.* 22, 387-394.
Du, J. and Axelbaum, R. L. (1995) *Combust. Flame* 100:367-375.
Du, J. and Axelbaum, R.L. (1996) *Proc. Combust. Inst.* 26, 1137-1142.
Glassman, I. and Takahashi F. (1984) *Comb. Sci. Tech.* 37:1-19.
Goldin, S. (1997) Public Address, NASA Lewis Research Center.
Gomez, A., Littman, M.G. and Glassman, I. (1987) *Combust. Flame* 70:225-241.
Grcar, J.F. (1992). The Twopnt Program for Boundary Value Problems, Sandia Report, SAND91-8230, Sandia National Laboratories.
Hirschfelder, J.O., Curtiss, C.F. and Bird, R.B., 1964, Molecular Theory of Gases and Liquids (Hoboken: Wiley and Sons).
Hwang, J.Y. and Chung, S.H. (2001) *Combust. Flame* 125:752-762.
Ishizuka, S. and Tsuji, H. (1981) *Proc. Combust. Inst.* 18, 695-703.
Kang, K.T., Hwang, J.Y. and Chung, S.H. (1997) *Combust. Flame* 109:266-281.
Kee, R.J., Dixon-Lewis, G., Warnatz, J., Coltrin, M.E. and Miller, J.A. (1988) A Fortran Computer Code Package for the Evaluation of Gas Phase Multicomponent Transport Properties. Sandia Report, SAND86-8246, Sandia National Laboratories.
Kee, R.J., Grcar, J.F., Smooke, M.D., Miller, J.A. and Meeks, E. (1987) A Program for Modeling Steady, Laminar, One-Dimensional Premixed Flames. Sandia Report SAND85-8240, Sandia National Laboratories.
Kee, R.J., Rupley, F.M. and Miller, J.A. (1989). Chemkin-II: A Fortran Chemical Kinetics Package for the Analysis of Gas Phase Chemical Kinetics, Sandia Report, SAND89-8009B, Sandia National Laboratories.
King, M.K. (1996) *Proc. Combust. Inst.* 26, 1227-1234.
Kumfer, B.M., Skeen, S.A. and Axelbaum, R.L. (2008) *Combust. Flame*, 154:546-556.
Kumfer, B.M., Skeen, S.A., Chen, R. and Axelbaum, R.L. (2006) *Combust. Flame* 147:233-242.
Law, C.K., Yoo, W.S., Christiansen, E.W. and Tse, S.D. (2001) Sixth International Microgravity Combustion Workshop, Cleveland, OH, May 22-24.

V.R. Lecoustre, P.B. Sunderland, B.H. Chao, D.L. Urban, D.P. Stocker, R.L. Axelbaum, 6th U.S. National Combustion Meeting, Ann Arbor (2009) 9 pp.
Lin, K.C. and Faeth, G.M. (1996) *J. Propulsion Power* 12(4):691-698.
Liu, S., Chao, B.H. and Axelbaum, R.L. (2005) *Combust. Flame* 140:1-23.
Macek, A. (1976) Flammability Limits: Thermodynamics and Kinetics, NBSIR Report 76-1076, National Bureau of Standards, Gaithersburg, Maryland.
Markatou, P. Wang, H. and Frenklach, M. (1993) *Combust. Flame* 93:467-482.
Maun, J.D., Sunderland, P.B. and Urban, D.L., "Thin-Filament Pyrometry with a Digital Still Camera," Applied Optics 46 (2007) 483-488.
McBride, B.J. and Gordon, S. (1996) Computer Program for Calculation of Complex Chemical Equilibrium Compositions and Applications. Report No. RP-1311-P2, NASA Lewis Research Center.
Middha, P., Yang, B. and Wang, H. (2002) *Proc. Combust. Inst.*, 29, 1361-1369.
Nayagam, V., Haggard, J.B., Colantonio, R.O., Marchese, A.J., Dryer, F.L., Zhang, B.L and Williams, F.A. (1998) AIAA J. 36 (8):1369-1378.
Okazaki, K. and Ando, T. (1997) *Energy*, 22:207-215.
Paul, P. and Warnatz, J., (1998), *Proc. Combust. Inst.* 27, 495–504.
Quintiere, J.G. (2006) Fundamentals of Fire Phenomena, Wiley, New York, p. 277.
Ronney, P.D., Wu, M.-S., Pearlman, H.G. and Weiland, K.J. (1998) *AIAA J.* 36(8):1361-1368.
Rothman, L.S., Rinsland, C.P., Goldman, A., Massie, S.T., Edwards, D.P., Flaud, J.-M., Perrin, A., Camy-Peyret, C., Dana, V., Mandin, J.-Y., Schroeder, J., Mccann, A., Gamache, R.R., Wattson, R.B., Yoshino, K., Chance, K.V., Jucks, K.W., Brown, L.R., Nemtchinov, V. and Varanasi, P. (2003) *J. Quantitative Spectroscopy and Radiative Transfer*, 82:5-44.
Santa, K.J., Chao, B.H., Sunderland, P.B., Urban, D.L., Stocker, D.P. and Axelbaum, R.L. (2007a), *Combust. Flame* 151:665-675.
Santa, K.J., Sun, Z., Chao, B.H., Sunderland, P.B., Axelbaum, R.L., Urban, D.L. and Stocker D.P. (2007b), *Combust. Theory Model* 11:639-652.
Santoro, R.J., Yeh, T.T., Horvath, J.J. and Semerjian, H.G. (1987) *Comb. Sci. and Tech.* 53:89-116.
Sekar, R.R., Marr, W.W., Assanis, D.N., Cole, R.L., Marciniak, T.J. and Schaus, J.E. (1991) *Journal of Engineering for Gas Turbines and Power,* 113:365-369.
Skeen, S.A., Yablonsky, G., Axelbaum, R.L., (2009), *Combust. Flame* 156:2145-2152.
Smith, G.P., Golden, D.M., Frenklach, M., Moriarty, N.W., Eiteneer, B., Goldenberg, M., Bowman, C.T., Hanson, R.K., Song, S., Gardiner Jr., W.C., Lissianski, V.V. and Qin, Z. (2007) available at http://www.me.berkeley.edu/gri_mech/.
Smooke, M.D., McEnally, C.S., Pfefferle, L.D., Hall, R.J. and Colket, M.B. (1999) *Combust. Flame* 117:117-139.
Sugiyama, G. (1994) *Proc. Combust. Inst.* 25, 601-608.
Sunderland, P.B., Axelbaum, R.L., Urban, D.L., Chao, B.H. and Liu, S. (2003) *Combust. Flame* 132:25-33.
Sunderland, P.B., Köylü, Ü.Ö. and Faeth, G.M. (1995) *Combust. Flame* 100:310-322.
Sunderland, P.B., Urban, D.L., Stocker, D.P., Chao, B.-H. and Axelbaum, R.L. (2004) *Comb. Sci. and Tech*, 176:2143-2164.
Sung, C.J., Liu, J.B. and Law, C.K. (1995) *Combust. Flame* 102:481-492.
Tse S.D., Zhu D.L., Sung C.J. Ju Y.G. and Law, C.K. (2001) *Combust. Flame*, 125(4):1265-1278.

Urban, D.L., Yuan, Z.-G, Sunderland, P.B., Linteris, G.T., Voss, J.E., Lin, K.-C., Dai, Z., Sun, K. and Faeth, G.M., (1998) "Structure and Soot Properties of Nonbuoyant Ethylene/Air Laminar Jet Diffusion Flames," *AIAA J.*, 36(8):1346.

Varagani, R., Chatel-Pelage, F., Pranda, P., Lu., Y., Chen, S., Rostam-Abadi, M., Farzan, H., Vecci, S.J. and Bose, A.C., (2004) Third Annual Conference on Carbon Sequestration, May 3-6, 2004, Alexandria, VA.

Villimpoc, V. and Goss, L.P. (1988) *Proc. Combust. Inst.* 22, 1907-1914.

Williams, F.A. (1981) Fire Safety J. 3:163-175.

Williams, S.J., Cuervo, L.A., and Chapman, M.A. (1989) High-Temperature Industrial Process Heating: Oxygen-Gas Combustion and Plasma Heating Systems, Gas Research Institute report GRI-89/0256, Chicago.

Yih, C.-S., Fluid Mechanics. McGraw Hill, NY, 1969, p. 107.

5 APPENDIX A

Estimate of Required Gravity Environment

The acceleration induced on a fluid packet by natural convection is

$$a = 2\frac{\rho - \rho_\infty}{2\rho + \rho_\infty} g_S = 2\frac{(\rho/\ \rho_\infty) - 1}{2(\rho/\ \rho_\infty) + 1} g_S \tag{A1}$$

where ρ is the density of the fluid packet, ρ_∞ the density of the fluid in the ambient, a the acceleration of the fluid packet, and g_S the gravitational acceleration (Yi *et al.*, 1969, Batchelor, 1983). Considering the flow to be isobaric and applying the ideal gas law, $p = \rho R T$ where p is the pressure and R the ideal gas constant, we have $\rho/\ \rho_\infty = T_\infty / T$. In a laboratory in the space station or a space shuttle, the gravity is caused by vibration so that it is taken to be periodic with amplitude A and frequency ω, given by $g_S = A \sin(2\pi\omega t)$, where t is the time. Adopting these assumptions, Eq. (B1) is modified to

$$a = A\frac{(T_\infty / T) - 1}{(T_\infty / T) + 0.5} \sin(2\pi\omega t)\ . \tag{A2}$$

Integrating Eq. (B2) yields the velocity of the fluid packet induced by gravity, given by

$$u = -\frac{A}{2\pi\omega}\frac{(T_\infty / T) - 1}{(T_\infty / T) + 0.5} \cos(2\pi\omega t) + c\ . \tag{A3}$$

If the acceleration starts at $t = 0$ so that $u = 0$ at $t = 0$, Eq. (B3) is changed to

$$u = \frac{A}{2\pi\omega}\frac{(T_\infty / T) - 1}{(T_\infty / T) + 0.5}[1 - \cos(2\pi\omega t)]\ . \tag{A4}$$

This gravity induced flow velocity introduces a modification of the mass flux of the reactant supplied from the burner, and consequently, a distortion of the flame shape from spherical symmetric. At the unperturbed flame front located at $r = r_f$, the normal component of the additional mass flux is

$$(\rho_f u_f)_n = \rho_f \frac{A}{2\pi\omega}\frac{(T_\infty / T_f) - 1}{(T_\infty / T_f) + 0.5}[1 - \cos(2\pi\omega t)](\cos\theta) \tag{A5}$$

where the subscript "*f*" denotes values at r_f, the subscript "*n*" denotes the normal component, and θ the angle with $\theta = 0$ along the direction of gravity, Since only the magnitude is of concern, the direction to define $\theta = 0$ or π is not important. The tangential component of the gravity induced flow velocity will not alter the reactant supply rate (consumption rate) at the flame front

and will be discarded.

For the mass flow rate of m, the mass flux at the flame front is $F = m / (4\pi r_f^2)$. Because the actual flame standoff distance depends linearly on the mass flow rate, if the maximum allowable distortion of the flame geometry from symmetrical symmetric is $\Delta r_f / r_f = \varepsilon$, we require $(\rho_f u_f)_n \le \varepsilon F$, or

$$\left| \rho_f \frac{A}{2\pi\omega} \frac{(T_\infty / T_f) - 1}{(T_\infty / T_f) + 0.5} [1 - \cos(2\pi\omega t)](\cos\theta) \right| \le \frac{\varepsilon m}{4\pi r_f^2} \quad . \tag{A6}$$

Since the maximum distortion occurs at $\cos(2\pi\omega t) = -1$ and $|\cos\theta| = 1$, as well as $T_\infty < T_f$, the maximum allowable gravity, expressed by A, can be reduced from Eq. (B6) to

$$A \le \frac{\varepsilon\omega m}{4\rho_f r_f^2} \frac{(T_\infty / T_f) + 0.5}{1 - (T_\infty / T_f)} \quad . \tag{A7}$$

Considering the fluid be sufficiently close to air, we approximate the fluid density by that of air such that the ideal gas equation of state gives $\rho_f = p / [(\overline{R} / M_a) T_f]$ where $\overline{R}$ is the universal gas constant and M_a the average molecular weight of the components (or air). Applying this approximation, Eq. (B7) is re-expressed in its final form by

$$\frac{A}{g} \le \frac{\varepsilon\omega m \overline{R} T_f}{4 g p M_a r_f^2} \frac{(T_\infty / T_f) + 0.5}{1 - (T_\infty / T_f)} = \frac{\varepsilon\omega m \overline{R}}{4 g p M_a r_f^2} \frac{T_\infty + 0.5 T_f}{1 - (T_\infty / T_f)} \quad , \tag{A8}$$

where g is the normal gravitational acceleration on earth. Taking $\overline{R}$ = 8.314 J/mole·K, M_a = 28.97 gm/mole (for air) and g = 9.8 m/s^2, Eq. (B8) is reduced to

$$\frac{A}{g} \le \left(0.07225 \frac{\text{mm}^2 \cdot \text{sec}^2 \cdot \text{atm}}{\text{gm} \cdot \text{K}} \right) \frac{\varepsilon\omega m}{p r_f^2} \frac{T_\infty + 0.5 T_f}{1 - (T_\infty / T_f)} \quad . \tag{A9}$$

In the space laboratory, the typical frequency of vibration is between 1 to 22 Hz (DeLombard, 1996). If the maximum allowable flame distortion is $\varepsilon = 0.1$, $p = 1$ atm, and adopting the most restrictive frequency of $\omega = 1$ Hz = 1 s^{-1}, Eq. (B9) is further reduced to

$$\frac{A}{g} \le \left(0.007225 \frac{\text{mm}^2 \cdot \text{sec}}{\text{gm} \cdot \text{K}} \right) \frac{m}{r_f^2} \frac{T_\infty + 0.5 T_f}{1 - (T_\infty / T_f)} \quad . \tag{A10}$$

Equation (B10) will then be applied to estimate the allowable gravity induced by vibration in the experiments, namely flames (a) – (d). In the following, T_∞ will be taken as 300 K while rf and Tf are results of the numerical calculations.

(1) Flame (a): m = 0.00151 gm/sec , Tf = 1477 K , rf = 17.72 mm

$\Rightarrow A/g = 4.53 \times 10^{-5}$ or $A = 4.53 \times 10^{-5}\ g = 45.3\ \mu g$

(2) Flame (b): m = 0.01855 gm/sec , Tf = 2021 K , rf = 9.40 mm

$\Rightarrow A/g = 2.37 \times 10^{-3}$ or $A = 2.37 \times 10^{-3}\ g$

(3) Flame (c): m = 0.02222 gm/sec , Tf = 2266 K , rf = 6.22 mm

$\Rightarrow A/g = 6.85 \times 10^{-3}$ or $A = 6.85 \times 10^{-3}\ g$

(4) Flame (d): m = 0.00518 gm/sec , Tf = 1572 K , rf = 16.23 mm

$\Rightarrow A/g = 1.91 \times 10^{-4}$ or $A = 1.91 \times 10^{-4}\ g = 191\ \mu g$

Among the 4 limiting cases, the most restrictive case is Flame (a). It is then concluded that for the flame distortion to be within an allowable 10% limit, the gravity level in the space laboratory should be lower than 45 μg. For other conditions, the allowable gravity level can be calculated using Eqs. (B8 or B9).